nature biomedical engineering

Article

https://doi.org/10.1038/s41551-026-01680-0

Modular peptide nanofibres that self-assemble on bacterial membranes overcome antimicrobial resistance

Received: 3 February 2024

Accepted: 8 April 2026

Published online: 20 May 2026

Check for updates

Ziao Zhou[1,4], Dinghao Chen[1,4], Jiang Ouyang[2,4], Nan Kong[1], Hongyue Zhang[1], Laicheng Zhou[1], Jing Wang[1], Tengyan Xu[1], Wei Chen[2], Na Kong[2,3], Wei Tao[2] ✉ & Huaimin Wang[1] ✉

Drug-resistant bacterial infections increasingly evade available antimicrobials, and many existing antimicrobial peptides remain limited by instability, toxicity to mammalian membranes and high manufacturing cost. Here we introduce a modular peptide technology that self-assembles into nanofibres on bacterial surfaces through a membrane-anchoring biphenyl group, a diphenylalanine linker and a cationic minimalistic peptide that together enable selective disruption of drug-resistant pathogens. Using cryogenic electron microscopy, molecular dynamics simulations, lipid-nanoparticle membrane mimetics and binding thermodynamics, we show that the peptide first forms short nanofibres that dock onto phosphatidylglycerol and then elongates into nanofibres that penetrate and destabilize the bacterial membrane without inducing resistance. The nanofibres retain antibacterial activity when recycled from killed bacteria and outperform vancomycin and several classical antimicrobial peptides against dense bacterial populations in vitro. In a mouse model of methicillin-resistant *Staphylococcus aureus* pneumonia, inhaled peptide nanofibres eradicate pulmonary infection and restore lung architecture without detectable toxicity. This modular strategy enables the design of potent, selective and low-cost antimicrobials.

The misuse and overuse of antibiotics have contributed to antimicrobial resistance worldwide, increasing mortality through the lack of effective therapeutics for drug-resistant infections[1–3]. Antimicrobial peptides (AMPs)—secreted by organisms in nature—may combat antimicrobial resistance pathogens[4], in addition to other strategies (antimicrobial metals, antimicrobial nanoparticles and antimicrobial polymers)[5–8]. Unlike conventional antibiotics, cationic AMPs kill bacteria through membrane lysis rather than acting on specific intracellular targets[9,10], hence minimizing the development of multidrug resistance.

There are obstacles to the clinical translation of AMPs, including (i) large molecular weight-caused high manufacturing costs and complex preparation[11,12], (ii) limited stability in vivo[13,14] and (iii) non-specific membrane binding affinity towards mammalian cells[15,16]. Cyclization can mitigate these limitations and improve the stability of AMPs in vivo[17]. In addition, chemical modifications of AMPs with additional moieties, such as glycosylation, fluorination and conjugation with fatty acid chains, have been used to increase the stability and antibacterial activity of AMPs[18–20]. Unfortunately, the systemic

[1]Zhejiang Key Laboratory of Precise Synthesis of Functional Molecules, Department of Chemistry, School of Science, Westlake University, Hangzhou, China. [2]Center for Nanomedicine and Department of Anesthesiology, Perioperative, and Pain Medicine, Brigham and Women's Hospital, Harvard Medical School, Boston, MA, USA. [3]Liangzhu Laboratory, Zhejiang University Medical Center, Hangzhou, China. [4]These authors contributed equally: Ziao Zhou, Dinghao Chen, Jiang Ouyang. ✉e-mail: wtao@bwh.harvard.edu; wanghuaimin@westlake.edu.cn

toxicity of these modifications may cause more damage than the infection itself[21–23].

To address these challenges, we developed a modular antimicrobial, Bip-FK9, for combating broad-spectrum multidrug-resistant bacteria and methicillin-resistant *Staphylococcus aureus* (MRSA) biofilms. The screened membrane target anchor in six anchors is a distinct N-terminal cap named Bip. Then, the minimalistic peptides of AMPs were conjugated to the Bip through a self-assembly promoting motif (FF), resulting in the creation of Bip-FK9 with a minimum inhibitory concentration (MIC) of 8 μM and a minimum bactericidal concentration (MBC) of 8 μM against MRSA. Our results indicated that the designed peptide can interact with the phosphatidylglycerol (PG), a phospholipid widely found on the bacterial membrane and rarely distributed in the plasma membrane of mammalian cells, producing selective killing of bacteria instead of mammalian cells. Cryo-electron microscopy (Cryo-EM) and all-atom molecular dynamics (MD) simulation showed that the peptide first self-assembled to form short nanofibres and then anchored on the cell membrane by anchor-navigated recognition. The formed short nanofibres penetrated the bacterial membrane to form long fibrous structures, which changed the permeability and potential of the membranes to induce MRSA death. Once the long nanofibres formed on the membrane, the treated bacteria subsequently exerted antibacterial activity, then intensively triggered substantial bacterial death. Compared with vancomycin (Van), Magainin II[24] and Ovispirin[22], the nanofibres showed better antibacterial activity in vitro. The self-assembling nanofibres are recyclable and reusable, further increasing their utility for killing bacteria. Moreover, in vivo experiments indicated that inhalable Bip-FK9 could combat MRSA-induced life-threatening lung infections in a mouse model by direct pulmonary deposition without causing acute toxicity or immune modulation.

Results and discussion

Construction of the Bip-FK9 and the transmembrane MD simulations of peptides

Membrane integrity disrupting strategies have proven efficient strategies to minimize drug resistance[25]. Thus, we hypothesized that using appropriate membrane-targeting anchors could guide the whole system to selectively target bacteria and assist the assembly of peptides on the membrane by an interface-induced self-assembly process. Specifically, the rationale for the general molecular structure design is based on the following components (Fig. 1a): (i) a bacterial membrane-targeting anchor for efficient recognition of phospholipid bilayers through hydrophobic interactions[26]; (ii) a minimalistic peptide derivative from AMPs of varied sources that promotes additional membrane binding and determines the efficiency of the whole system against MRSA[4,27]; (iii) a self-assembly linker for controlling the anchoring capability of the peptide and promoting the whole system's self-assembly[28–34]. We chose the minimalistic peptides from existing peptide resources (including host defence peptides, AMPs under clinical investigation and peptides shown in the APD3 Antimicrobial Peptide Database)[35–37]. These minimalistic peptides consisted of 6–10 amino acids and were characterized by a net positive charge ranging from +3 to +6, a high proportion of hydrophobic residues and the absence of acidic residues. We screened six capping groups (Fig. 1a) from the well-known hydrophobic self-assembly promoting motif (Nap, Ada and Oct) or the key segments of antimicrobial agents (Bip, Chl and Iso)[38–41]. First, to pick out the best N-terminal groups in six N-terminal groups, the antibacterial activity of FK9 modified with these N-terminal groups was tested (Fig. 1b). The anti-MRSA activity of Bip conjugation was much higher than that of the peptide itself and others. In addition, the fluorescence intensity of 1-(*N*-phenylamino)naphthalene (NPN), a lipophilic fluorescent dye, is greatly enhanced when the membrane is damaged[42]. The fluorescence intensity of NPN in the Bip-FK9 group was greater than in other groups (Fig. 1c), suggesting that Bip-FK9 achieved the greatest destruction of bacterial membranes. These results indicated that Bip was the most efficient N-terminal group for killing MRSA, as evidenced by bacterial viability assay and NPN assay.

Next, MD simulations of the transmembrane process of different N-capping peptides[43,44] (Supplementary Videos 1–7) were used to elucidate the possible mechanism of the superior antimicrobial activity of the Bip group. By observing the different conformations of peptides and the membrane in MD simulations (Fig. 1d and Extended Data Fig. 1a), we found that Bip-FK9 was more prone to embed into the membrane to stimulate subsequent perturbation, and the centroid distance between Bip-FK9 and phospholipid bilayers was the shortest in all the experimental groups (Fig. 1e). Meanwhile, compared with the peptides (except Nap-FK9), Bip-FK9 has a larger contact area with the cell membrane and lower binding energy (Extended Data Fig. 1b,c). Cavity assessment indicated that Bip-FK9 possessed the largest cavity volume and achieved the most intensive insertion on the membrane (Fig. 1f,g and Supplementary Fig. 1). These results revealed that the Bip was the best capping group for minimalistic peptides to interact with the bacterial membrane for killing bacteria.

Characterization of Bip-FK9 and its antibacterial activity in vitro

Circular dichroism (CD) spectra (Fig. 2a) showed that Bip-FK9 formed a β-sheet-like structure, which was evidenced by a positive peak at 195 nm and a negative peak at 212 nm. By contrast, K7 and Bip-FF formed no obvious secondary structures. Cryo-EM images indicated that Bip-FK9 and Bip-FF self-assembled to form nanofibres, and K7 cannot form nanostructures (Fig. 2b and Extended Data Fig. 2a).

Next, we performed concentration-dependent and time-dependent killing experiments to evaluate the long-term antibacterial effects of Bip-FK9 and whether the bacteria regenerated after Bip-FK9 treatment. The results (Fig. 2c and Extended Data Fig. 2b) indicated that Bip-FK9 at the concentration of 32 μM inhibited bacterial growth during the test period. The spread plate method showed that the MRSA concentration in the Bip-FK9 treatment group decreased by 5 orders of magnitude compared with the control group at 8 h (Extended Data Fig. 2c). Biofilm formation is an important factor in antibiotic resistance and infection recurrence. We evaluated whether Bip-FK9 could eradicate MRSA-formed biofilms (Fig. 2d). These results indicated that Bip-FK9 could disrupt the formed biofilm and inhibit the growth of MRSA. Then, we used the field emission scanning electron microscope (FE-SEM) to observe the morphologic changes in MRSA after treatment with Bip-FK9 and found that unlike what was seen in control groups (Fig. 2e), the structures formed by Bip-FK9 attached to the surface of the MRSA and encapsulated it, which could be interpreted as the bacteria being completely captured and killed. Confocal microscopy images (Fig. 2f and Extended Data Fig. 2d) of live–dead assay also demonstrated that Bip-FK9 had good penetration and killing effect on biofilms. Finally, resistance-acquisition studies (Fig. 2g) suggested that MRSA did not generate resistance in 30 continuous passages of Bip-FK9 exposure. By contrast, MRSA began to develop resistance to the antibiotic ciprofloxacin (Cip) after five passages, suggesting that the Bip-FK9 killed MRSA without eliciting any detectable resistance.

The superiority of Bip-FK9 for killing substantial MRSA over antibiotics (Van) and classical AMPs

To evaluate the ability of Bip-FK9 against high-concentration MRSA, we performed the experiments illustrated in Fig. 2h. MRSA (1×10^8 CFU ml^{-1}) was mixed with Bip-FK9 (128 μM) and co-incubated for 4 h. The results showed (Fig. 2i) that MRSA (1×10^8 CFU ml^{-1}) was eradicated by Bip-FK9. Next, we used a centrifuge to separate the precipitates and the supernatants from the solution formed by MRSA treated with Bip-FK9, in which all the MRSA were killed (Fig. 2i). The precipitates, consisting of dead MRSA and Bip-FK9 (denoted as Bip-FK9-MRSA), could kill 98.32% of a new fresh batch of MRSA (Fig. 2j). The presence of Bip-FK9 nanofibres on the dead MRSA exhibited notable antibacterial

https://doi.org/10.1038/s41551-026-01680-0

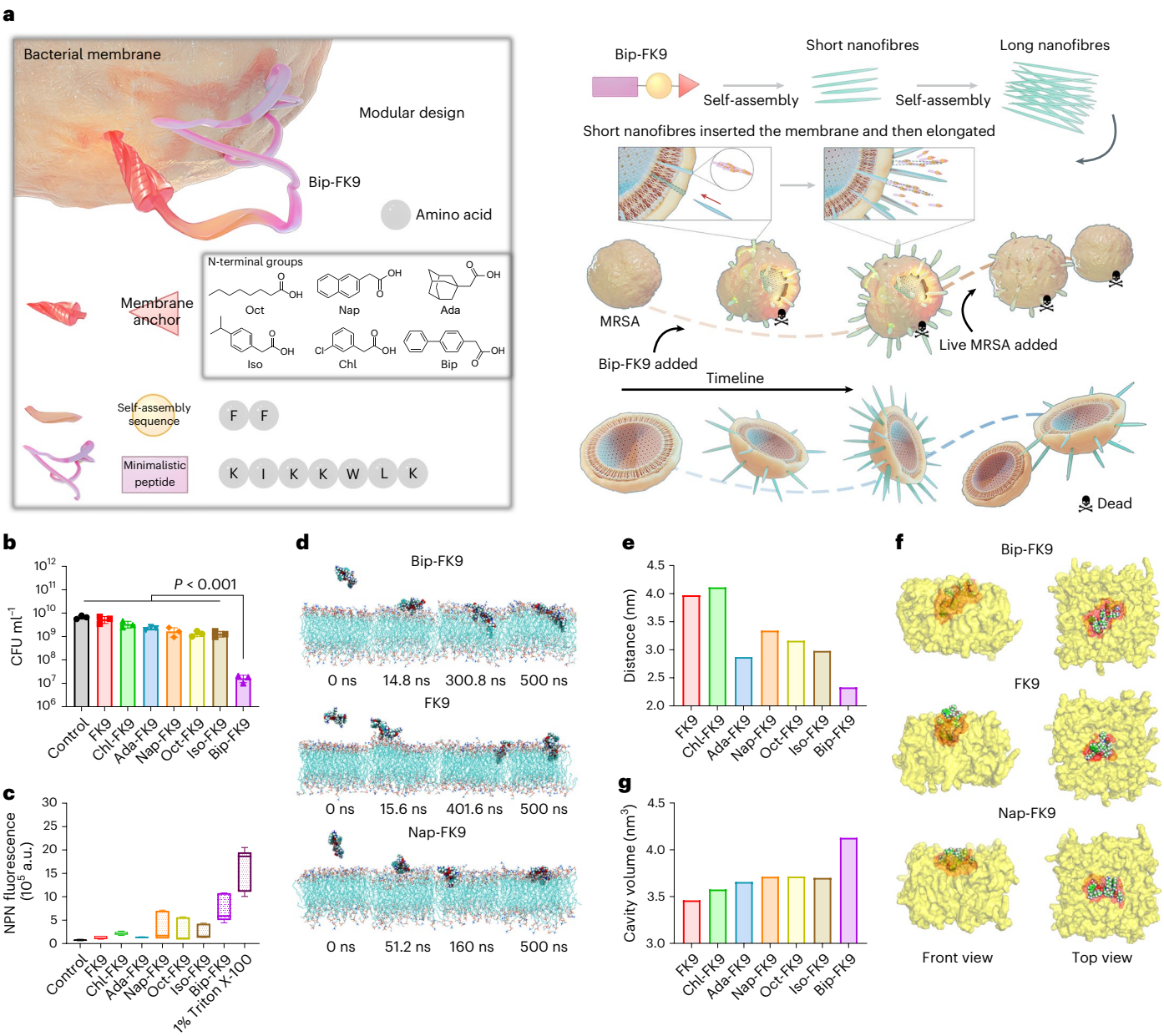

Fig. 1 | Modular design of Bip-FK9 for combating MRSA and MD simulation of FK9 and FK9 modified with different membrane anchors. a, Illustration of a design principle for Bip-FK9, which consists of a suitable membrane anchor at the N-terminal of peptides, a self-assembly promoting motif (FF) and a minimalistic peptide from the peptide library. The minimalistic peptides were selected and truncated from naturally available sources (host defence peptides, peptides in clinical trials and the peptides in the APD3 Antimicrobial Peptide Database). The illustration on the right shows the growing processes of fibrous structures that cross through bacterial membranes and elongate along the membrane surface. Once the nanofibres form on MRSA, the treated MRSA can kill a new batch of MRSA. **b**, The viability of MRSA after treatment with different anchor-modified peptides (8 μM) for 24 h. FK9, FFKIKKWLK; Chl-FK9, Chl-FFKIKKWLK; Ada-FK9, Ada-FFKIKKWLK; Nap-FK9, Nap-FFKIKKWLK; Oct-FK9, Oct-FFKIKKWLK; Iso-FK9, Iso-FFKIKKWLK. The data are presented as mean ± s.d. ($n = 3$). **c**, The membrane integrity of MRSA was measured via NPN uptake assay. The data are presented as mean ± s.d. ($n = 6$). **d**, Representative results of MD simulations to show the interactions between Bip-FK9, FK9 and Nap-FK9 with the lipid bilayer, respectively. Different time points indicate the beginning stage, the membrane approach, the membrane penetration and the equilibrium stage, respectively. The lipid bilayer was constructed by PC:PG (7:3). **e**, Calculated distance between the centroid of peptides and the lipid bilayer at an equilibrium stage in MD simulations. **f**, Representative configurations of peptides and the bilayer at an equilibrium stage in MD simulations. **g**, Cavity volume on lipid bilayer generated by the membrane insertion of peptides at an equilibrium stage in MD simulations. Statistical significance in **b** was determined using an unpaired, two-tailed Student's *t*-test.

activity, leading to substantial bacterial death. In another parallel experiment, we extracted Bip-FK9 from the surface of the dead MRSA using water adjusted to pH 4, then neutralized the solution to pH 7.4. We co-incubated the treated MRSA, which no longer had Bip-FK9, with a new batch of MRSA (1×10^8 CFU ml^{-1}) for 8 h (Extended Data Fig. 2e). The results showed that the treated MRSA could not kill MRSA. By contrast, when we co-incubated the recycled Bip-FK9 with a fresh batch of MRSA (1×10^8 CFU ml^{-1}) for 8 h (Fig. 2k), nearly all bacteria (99.9998%) were killed by Bip-FK9, indicating that it retained its antibacterial properties after recycling. In addition, our findings demonstrated that Bip-FK9 can be cycled efficiently to kill MRSA up to six times (Extended Data Fig. 2f).

To evaluate the rapid antibacterial efficacy of Bip-FK9, we co-incubated MRSA (1×10^8 CFU ml^{-1}) with the classical AMPs and Bip-FK9 for 120 min, respectively (Extended Data Fig. 2g). Bip-FK9

https://doi.org/10.1038/s41551-026-01680-0

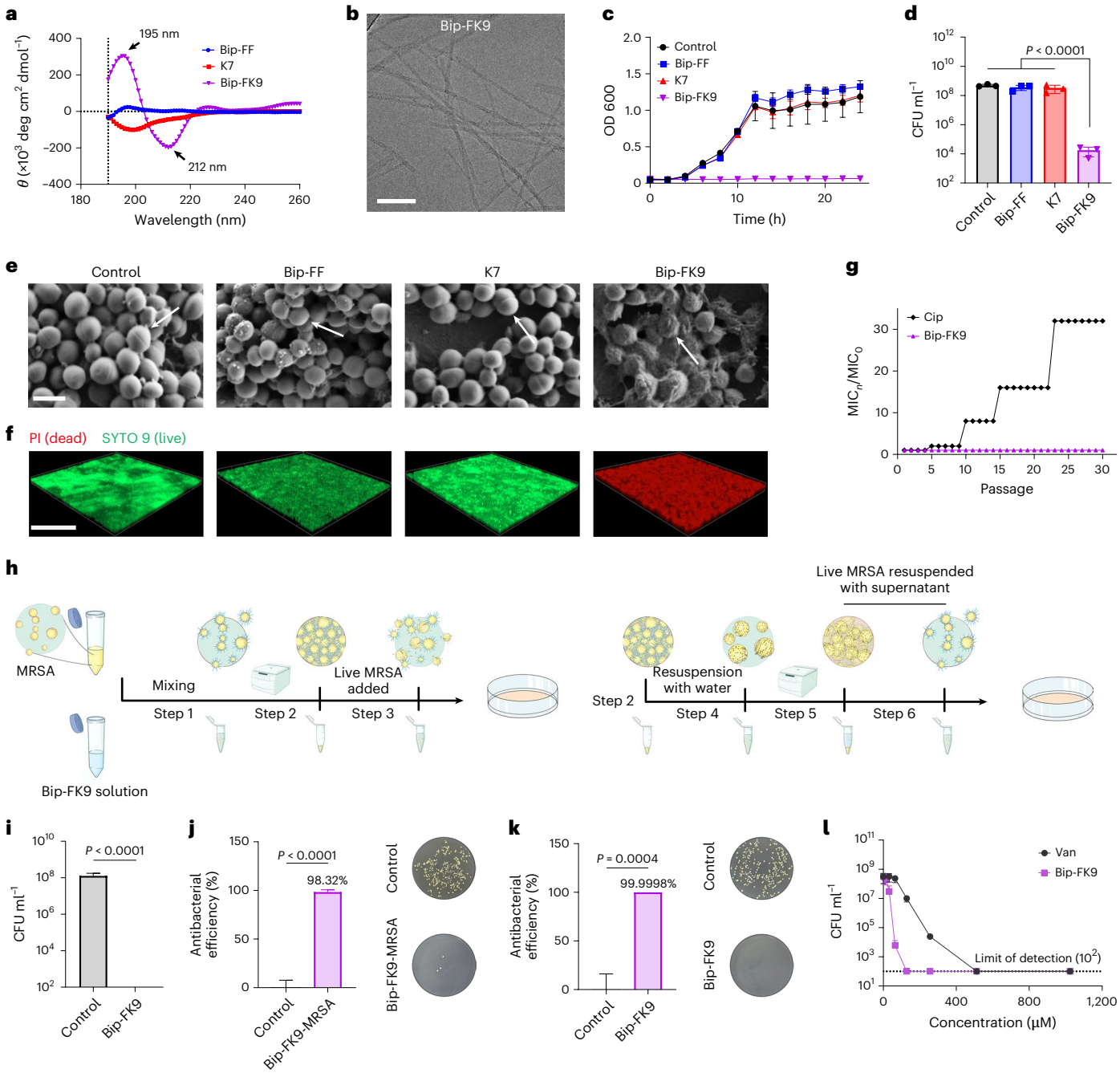

Fig. 2 | Characterization of Bip-FK9 and its bactericidal activity in vitro. a, CD spectra of Bip-FF, K7 and Bip-FK9. **b**, The Cryo-EM image of Bip-FK9 (128 μM) in the PBS buffer. Scale bar, 100 nm. **c**, Time-dependent growth curves of MRSA treated with different peptides (32 μM). The data are presented as mean ± s.d. ($n = 3$). **d**, The viability of MRSA biofilm treated with the peptides for 4 h. **e**, The FE-SEM images of MRSA biofilm under the treatment of Bip-FF, K7 and Bip-FK9. Scale bar, 1 μm. **f**, The laser confocal fluorescence microscopy images of MRSA biofilm under the treatment of Bip-FF, K7 and Bip-FK9. Live bacteria are stained with SYTO9 (green), and dead bacteria are stained with PI (red). Scale bar, 160 μm. **g**, Resistance-acquisition studies of MRSA subjected to Bip-FK9 and Cip treatment at the concentration of sub-MIC (1/2×). **h**, Schematic illustration showing that Bip-FK9 could kill the MRSA, and the treated MRSA subsequently exerted antibacterial activity, then intensively triggered substantial bacterial death. Bip-FK9 could be recycled to kill a new batch of MRSA. Step 1, MRSA were mixed with Bip-FK9 solution (pH = 7.4) in a 1.5 ml EP tube; step 2, centrifuge the EP tube and remove the supernatant; step 3, a new batch of MRSA solution was added to the EP tube; step 4, resuspend MRSA precipitation with water (pH = 4) in a 1.5 ml EP tube for dissolving Bip-FK9 on the surface of MRSA; step 5, centrifuge the EP tube and collect the supernatant; step 6, adjust the pH of the supernatant to 7.4, and then live MRSA resuspended with the supernatant. **i**, The viability of planktonic MRSA (1×10^8 CFU ml^{-1}) incubated with Bip-FK9 at the concentration of 128 μM. After the co-incubation, a 10 μl mixture was used for CFU quantification via the spread plate method. **j**, Viability of planktonic MRSA incubated with Bip-FK9-MRSA for 8 h. After Bip-FK9 killed the MRSA, the MRSA with Bip-FK9 nanofibres was named Bip-FK9-MRSA. The corresponding LB agar plates are shown on the right. Bip-FK9 nanofibres on the MRSA can kill a new batch of MRSA. **k**, Antibacterial studies of recyclable Bip-FK9. Bip-FK9-MRSA was dissolved in water (pH = 4) and centrifuged to remove MRSA. The pH of the supernatant was adjusted to 7.4. Next, the supernatant containing Bip-FK9 was incubated with MRSA for 8 h, resulting in high antibacterial efficiency. The corresponding LB agar plates are shown on the right. **l**, Colony-forming units (CFU ml^{-1}) of MRSA treated with Van or Bip-FK9 at different concentrations, respectively. The data are presented as mean ± s.d. ($n = 3$). Statistical significance in **d** and **i**–**k** was determined using an unpaired, two-tailed Student's *t*-test, and individual data are presented as mean ± s.d. ($n = 3$).

reduced the MRSA concentration to the limit of detection within 60 min, whereas Melittin required 5 min, OP-145 took 30 min, and Pexiganan acetate and Ovispirin each took 60 min to achieve the same reduction. Next, we evaluated the toxicity of these peptides against A549 cells. Bip-FK9 maintained over 90% cell viability, whereas Melittin and Ovispirin exhibited less than 30% cell viability. Pexiganan acetate and OP-145 showed intermediate cell viability, ranging between 50% and 80%. These results indicated that, while maintaining good biocompatibility, Bip-FK9 exhibited faster antibacterial activity than the classical AMPs. In addition, we also compared the antimicrobial activity of Bip-FK9 and Van (bacteriostat). Bip-FK9 at a series of concentrations and Van at a series of concentrations were mixed with MRSA (1×10^8 CFU ml^{-1}), respectively, and co-incubated for 18 h (Fig. 2l). Our results indicated that Bip-FK9 at a concentration of 128 μM reduced the MRSA concentration to the limit of detection, whereas Van required a concentration of 512 μM to achieve the same reduction. The concentration of Bip-FK9 was lower when it achieved the same antibacterial effect as Van. These results demonstrated that Bip-FK9 had excellent antibacterial activity.

The antibacterial mechanism of Bip-FK9

First, we used a cryo-electron microscope (Cryo-EM) to investigate the morphological changes in MRSA before and after incubation with Bip-FK9 (Fig. 3a,b). The untreated MRSA and the MRSA treated with two peptides (Bip-FF and K7) exhibited smooth surfaces. By contrast, Bip-FK9 formed tiny nanofibres on the surface of MRSA, which gradually became more numerous and elongated over time. This bacterial phenotype may suggest that short Bip-FK9 nanofibres can closely interact with the membrane through hydrophobic interactions and then self-assemble to form long nanofibres on the cell surface. The long Bip-FK9 nanofibres can also directly interact with the bacterial membrane. Next, we evaluated membrane integrity and the metabolism of bacteria treated with peptides. We found that the PI fluorescence intensity of MRSA under the treatment of Bip-FK9 increased. The ATP level of MRSA treated with Bip-FK9 decreased (Fig. 3c and Extended Data Fig. 2h). We also evaluated the survival status of MRSA treated with the Bip-FK9 and found that 99.9998% of MRSA was killed by Bip-FK9 at 10 min (Extended Data Fig. 2i). These results suggested that the nanofibres on the cell surface could change the integrity of cell membrane, affect bacterial metabolism and contribute to MRSA death. In addition, we used the reactive oxygen species (ROS) probe DCFH-DA to assess ROS levels in MRSA (Extended Data Fig. 2j). Compared with the control group, the fluorescence intensity of the ROS probe in the Bip-FK9 group increased by approximately twofold, indicating that Bip-FK9 elevated ROS levels in MRSA, thereby further exacerbating bacterial membrane damage[45].

Next, we focused on the efficacy of Bip-FK9 on the bacterial membrane. Membrane potential[45] (Fig. 3d) measurement by $DiSC_3(5)$ showed that Bip-FK9 thoroughly depolarized the bacterial membrane after co-incubation with MRSA, suggesting that the nanofibres formed by Bip-FK9 affected the membrane potential. We also constructed simplified *S. aureus* membranes by formulating liposomal nanoparticles (LNPs) to study the interactions between Bip-FK9 and bacterial membranes[46,47] (Fig. 3e and Extended Data Fig. 3a). The zeta-potential results indicated that the interaction involved electrostatic interactions (Fig. 3f and Extended Data Fig. 3b). After the addition of Bip-FK9, the strong interaction between LNPs and Bip-FK9 resulted in dehydration, aggregation and precipitation of LNPs[48] (Extended Data Fig. 3c,d), which caused the characteristic peaks of the CD spectrum in the LNPs + Bip-FK9 group to disappear (Fig. 3g). The transmission electron microscopy (TEM) images showed that the structure of LNPs was destroyed, clumped together and surrounded by Bip-FK9 nanofibres (Extended Data Fig. 3e). These results demonstrated that Bip-FK9 could interact with LNPs.

The addition of bacterial wall components (lipoteichoic acid (LTA) and peptidoglycan (PepGly))[49] did not abolish the activity of Bip-FK9 against MRSA (Fig. 3h), suggesting that the antibacterial activity of Bip-FK9 was not due to the interaction between Bip-FK9 and bacterial wall components. However, among the main components (lysylphosphatidylglycerol (Lysyl-PG), cardiolipin (CL), phosphatidic acid (PA) and PG) of the bacterial membrane[50], the addition of PG notably improved the survival rate of bacteria as the treatment of Bip-FK9 (Fig. 3i,j), suggesting that Bip-FK9 cannot bind to PG on the bacterial membrane after binding to free PG in solution, resulting in decreased antibacterial activity of Bip-FK9. PG was the main target of Bip-FK9. Isothermal titration calorimetry (ITC) experiments showed that the dissociation constant (K_D) of Bip-FK9 and PG was 8.49×10^{-2} μM (Fig. 3k), suggesting a high binding affinity between them.

To further demonstrate the interaction between Bip-FK9 and PG, NMR experiments were performed using fluoro-modified Bip-FK9 (BipF-FK9). Transverse relaxation (T2) of peptide dropped from 1788.12 ms to 74.32 ms in ^{19}F spectrum in the presence of PG (Fig. 3l), indicating that BipF-FK9 binding to PG resulted in greater molecular weight and slower molecular movement. By comparing the intramolecular ^{1}H–^{1}H NOESY correlation spectra of BipF-FK9 (Fig. 3m), several NOE cross-peaks correlating BipF-FK9 with PG can be observed (Fig. 3n). The increased intermolecular NOE signals support the proximity of BipF-FK9 and PG molecules. Specifically, the proton neighbouring alkenyl and CH_2 protons in dioleoyl of PG had NOE effects with the biphenyl proton of BipF-FK9, suggesting the interaction between biphenyl of BipF-FK9 and dioleoyl of PG.

Dynamic insertion of the Bip-FK9 nanofibres on bacterial membrane

To deeply understand how Bip-FK9 could fiberize and embed into bacterial membrane, MD simulation was applied to elucidate the molecular interaction between nanofibres and lipid bilayer. First, the fast, stable assembling process of Bip-FK9 nanofibres was simulated (Extended Data Fig. 4a–c). MD simulations showed that Bip-FK9 self-assembled to form stable assemblies after 10 ns (Fig. 4a). The root-mean-square deviation (RMSD) of the system was stable at about 4 nm and fluctuated in the range of 1 nm. The complex tended to be stable in the solvent system, which was consistent with the results of root-mean-square fluctuation (RMSF) analysis (Fig. 4b,c). Snapshots at different time points suggested that Bip-FK9 underwent structural adjustment, migration and gradual self-aggregation and reached a stable equilibrium state without dissociation (Supplementary Video 8). Bip-FK9 molecules assembled each other and formed nanofibres through hydrogen bond interactions and π–π stacking (Extended Data Fig. 4d). The conformational snapshots revealed the stability of nanofibres, which was consistent with the results of the two-dimensional (2D) density of the system during the kinetic simulation (Supplementary Fig. 2). At 0 ns, Bip-FK9 molecules were dispersed in water, maintaining distance from one another. As the simulation progressed, the hydrophobic portion (Bip-FF) of Bip-FK9 repelled water molecules owing to hydrophobic interactions, causing the peptides to move closer together. This led to the formation of hydrogen bonds between Bip-FK9 molecules, which gradually increased and ultimately stabilized (Fig. 4d). Conversely, the number of hydrogen bonds between Bip-FK9 and water molecules decreased over time, reflecting a reduced binding surface area for interaction with water as the peptides assembled into nanofibres (Fig. 4e). The solvent-accessible surface area (SASA) of the whole system gradually declined and finally reached a steady state (Fig. 4f). Bip-FK9 nanofibres formed and stabilized. These kinetic simulation results indicated that assemblies of Bip-FK9 could form rapidly and remain stable in an aqueous solution.

Stepping on the findings above, we moved to the next stage of exploring the specific mechanism facilitating the interaction between nanofibres and bacterial membrane. The stable insertion process of the Bip-FK9 nanofibre into the membrane was simulated (Extended Data Fig. 4e–g). MD simulations showed that the nanofibres

https://doi.org/10.1038/s41551-026-01680-0

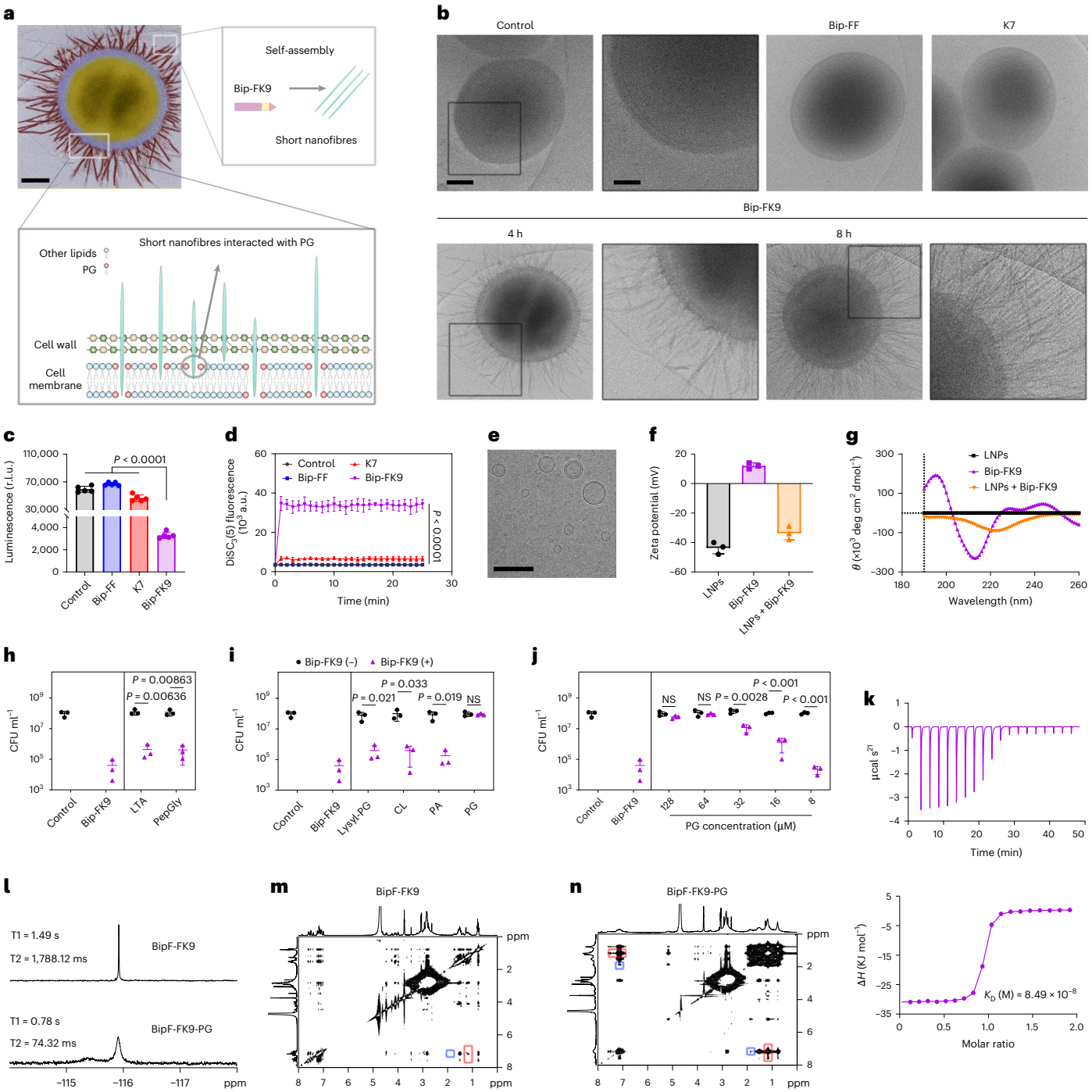

Fig. 3 | The antibacterial mechanism of Bip-FK9. a, Illustration of the interaction between Bip-FK9 and the MRSA membrane. After 4 h of co-incubation, the assemblies of Bip-FK9 were inserted into the bacterial cell membrane. The small nanofibres can interact with the PG of the bacterial membrane. Scale bar, 200 nm. **b**, Cryo-EM images of MRSA exposed to different peptides for 4 h and 8 h. Scale bar, 200 nm. Scale bar in the magnified image, 400 nm. **c**, Intracellular levels of ATP from the MRSA with the treatment of peptides. Individual data are presented as mean ± s.d. ($n = 5$). **d**, Bacterial membrane depolarization effects of peptides towards MRSA. Individual data are presented as mean ± s.d. ($n = 3$). **e**, Cryo-EM images of LNPs consisting of PC:PG = 7:3. Scale bar, 200 nm. **f**, Zeta potential of LNPs, Bip-FK9 and the mixture of LNPs and Bip-FK9. **g**, CD spectra of LNPs, Bip-FK9 and the mixture of LNPs and Bip-FK9. **h**,**i**, Changes in bacterial concentrations after the treatment of Bip-FK9 in the presence of different bacterial wall components (**h**) and bacterial membrane components (**i**). Individual data are presented as mean ± s.d. ($n = 3$). **j**, Changes in bacterial concentrations after the treatment of Bip-FK9 in the presence of PG at different concentrations. Individual data are presented as mean ± s.d. ($n = 3$). **k**, The ITC analysis of the interaction between Bip-FK9 and PG. The dissociation constant K_D values of Bip-FK9 to PG was 8.49×10^{-8} M. **l**, ^{19}F spectra of BipF-FK9 and BipF-FK9-PG. **m**, The NOESY spectrum of BipF-FK9. **n**, The NOESY spectrum of BipF-FK9-PG. Statistical analysis in **c**, **d** and **h**–**j** was determined using an unpaired, two-tailed Student's *t*-test. NS, not significant.

of Bip-FK9 were gradually inserted into the membrane to maintain stable conformation without dissociation (Fig. 4g and Supplementary Video 9). After interacting with the membrane, the nanofibres underwent structural adjustment to reach a penetrating state (Fig. 4h). Figure 4i shows that the hydrogen bond interaction and hydrophobic interaction between the Bip-FK9 molecules in the nanofibres and PG molecules in phospholipid layers were formed in the Bip-FK9-BM system at 50 ns. During the simulation (Fig. 4j), the nanofibres were

https://doi.org/10.1038/s41551-026-01680-0

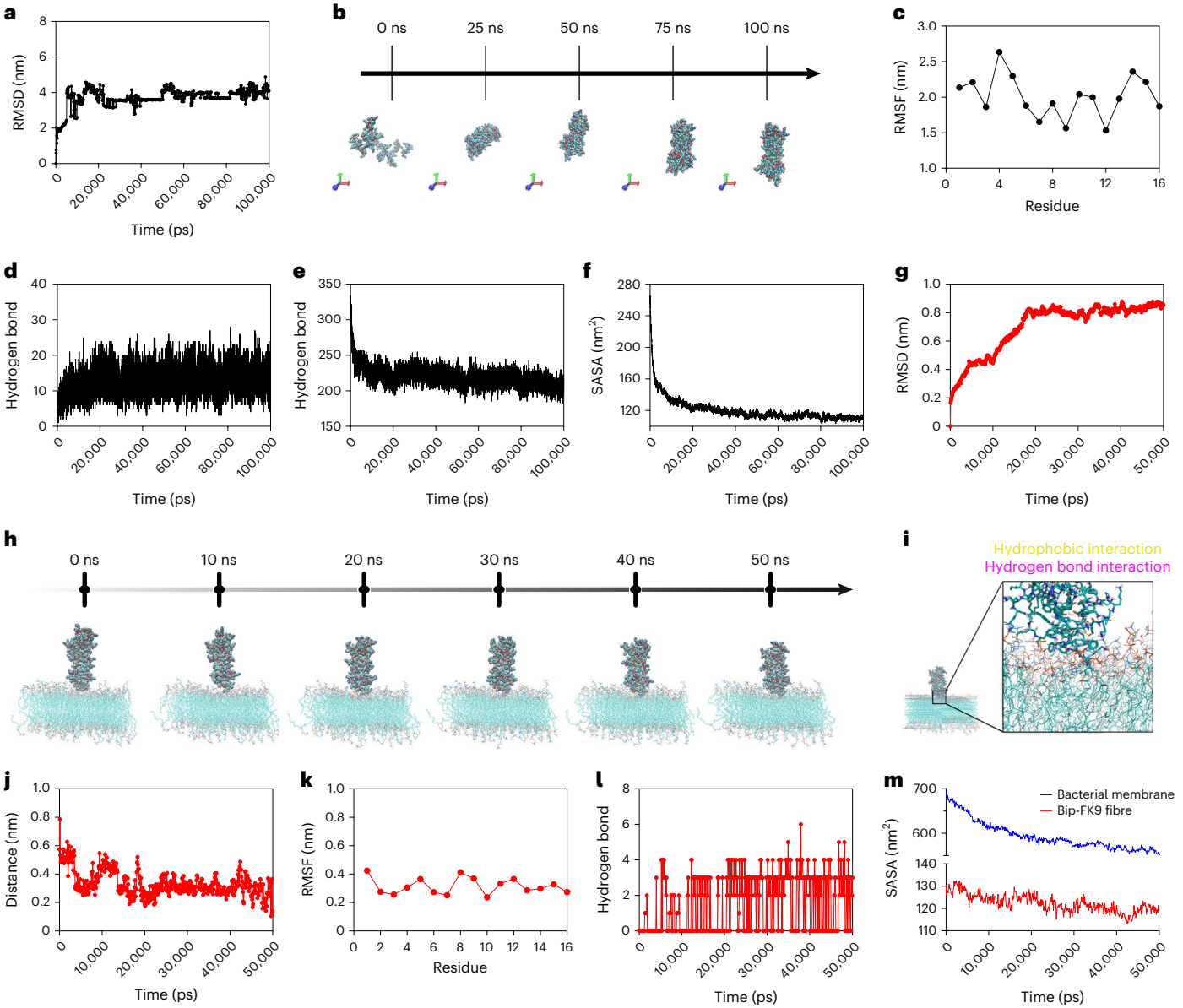

Fig. 4 | Dynamic insertion of the Bip-FK9 nanofibres into the bacterial membrane (BM). a, The RMSD of the Bip-FK9 self-assembly model to assess their stability in processes of MD simulation (100 ns). In this process, the equilibrium time point was determined by RMSD as its value stabled at near 4 nm after 10 ns, within 1 nm fluctuation, indicating that a steady state was reached. **b**, Representative configurations of Bip-FK9 self-assembly processes in MD simulation at 0 ns, 25 ns, 50 ns, 75 ns and 100 ns. **c**, The RMSF of residues of the Bip-FK9 self-assembly model over the time to characterize the degree of change in the structure of matter. **d**,**e**, The changes in hydrogen bonds of the system. The intermolecular hydrogen bonds in Bip-FK9 nanofibres (**d**) and the number of hydrogen bonds between peptide molecules and water (**e**) are shown here. **f**, The SASA of Bip-FK9 in self-assembly processes. **g**, RMSD of the Bip-FK9-BM model to assess their stability in the MD simulation (50 ns) process. **h**, MD simulation results of the dynamic conformation changes of Bip-FK9 nanofibres on the bacterial membrane surface at 0 ns, 10 ns, 20 ns, 30 ns, 40 ns and 50 ns. **i**, Magnified view of the conformation of the interaction between the Bip-FK9 nanofibre and the phospholipid bilayer in the Bip-FK9-BM system at 50 ns. Hydrophobic interaction (yellow dots); hydrogen bond interaction (purple dots); PG molecules (greyness). **j**, Distance between Bip-FK9 nanofibres and the lipid bilayer in the MD simulation. **k**, RMSF of residues of the Bip-FK9-BM system. **l**, Hydrogen bonds between Bip-FK9 nanofibres and the lipid bilayer. **m**, SASA of the Bip-FK9-BM system in the MD simulation.

gradually inserted into one side of the phospholipid bilayer and remained stable until the distance between them approached 0.1 nm. The flexibility test demonstrated that the nanofibre formed a tight attachment to the phospholipid bilayer, as the final RMSF maintained a value smaller than 0.4 nm (Fig. 4k). The stabilization of the hydrogen bond quantity at approximately 50,000 ps supported the conclusion that the nanofibres exhibited strong hydrogen bond interactions with the membrane via gradual infiltration, thereby ensuring their stability on the membrane surface (Fig. 4l). The SASA of the phospholipid bilayer and the Bip-FK9 nanofibres gradually decreased and eventually reached a steady state, producing similar results (Fig. 4m). These results suggested that the peptide nanofibres were unable to dissociate from the membrane.

In vitro biocompatibility of Bip-FK9 and the mechanism of action of Bip-FK9 on mammalian cell

Before investigating the antibacterial activity of Bip-FK9 in treating infections in animals, the cytotoxicity of Bip-FK9 towards two mammalian cells was evaluated[51] (Extended Data Fig. 5a). The results indicated that the peptides had no apparent cytotoxicity to A549 cells (lung carcinoma epithelial cell line) or RAW 264.7 cells (mouse macrophages). Haemolysis tests (Extended Data Fig. 5b) showed that the haemolytic rate of

red blood cells induced by Bip-FK9 was less than 5% at the concentration of 320 μM, 40-fold larger than the MIC of MRSA. Next, to investigate the effects of Bip-FK9 on the A549 cell membrane, we used confocal laser scanning microscopes (CLSM) to observe the integrity of the cell membrane by staining the cell membrane with a commercial tracker (Extended Data Fig. 5c). Notably, the cells treated with 0.1% Triton X-100 exhibited membrane damage, allowing BOBO 3-Iodide to enter the cells and stain nucleic acids. By contrast, A549 cells treated with Bip-FK9 showed intact membranes, preventing BOBO 3-Iodide from entering and staining nucleic acids. The mammalian cell membrane is predominantly composed of cholesterol and phospholipids. The representative phospholipid components of the mammalian plasma membrane[52] and the *S. aureus* membrane[50] are shown in Extended Data Fig. 5d. We mixed these mammalian cell membrane components with MRSA, followed by the addition of Bip-FK9 (Extended Data Fig. 5e). The results showed that PS had no antibacterial activity. However, when PS was included in the mixture containing MRSA and Bip-FK9, the concentration of MRSA in the Bip-FK9 + PS group increased approximately 100-fold compared with the Bip-FK9-only treated group. PS could inhibit the antibacterial activity of Bip-FK9, which indicated that PS can interact with Bip-FK9. We measured the dissociation constants of Bip-FK9 for PS and PG using an ITC instrument (Fig. 3k, Extended Data Fig. 5f and Supplementary Fig. 3). The results indicated a stronger binding affinity of Bip-FK9 for PG compared with PS. Furthermore, PS is rarely present on the surface of mammalian cells, primarily residing in the inner leaflet of the plasma membrane[53]. In exceptional cases, such as apoptosis and internalization of the virus, PS was translocated from the inner leaflet of the plasma membranes to the outer leaflet of the plasma membranes and finally exposed to the surface of mammalian cells. Therefore, Bip-FK9 could not target the PS in the normal plasma membranes. TEM was used to observe the morphology of A549 cells treated with Bip-FK9 (Extended Data Fig. 5g). The TEM images confirmed that Bip-FK9 did not destroy the integrity of the A549 cell membranes.

Biosafety in vivo and biodistribution

To test the biosafety of Bip-FK9 in mice, we treated the mice with Bip-FK9 twice a day by nebulization for 7 consecutive days. No notable body weight loss was observed (Fig. 5a). Bronchoalveolar lavage fluid (BALF) was extracted from mouse lungs to analyse cytokines and cell sorting (Fig. 5b,c and Extended Data Fig. 6a). There were no changes in the production of cytokines (tumour necrosis factor (TNF)-α, interleukin (IL)-6, IL-12, IL-4 and IL-10) of BALF in the Bip-FK9 group compared with that in the 0.9% saline group. In vitro macrophage polarization assay also suggested that Bip-FK9 did not change the polarity of macrophages (Extended Data Fig. 6b–d). In addition, we observed no increase in allergy markers (IgE and IgG) (Extended Data Fig. 6e,f), indicating that Bip-FK9 had low immunogenicity. Finally, haematoxylin and eosin (H&E) staining images of major organs (Fig. 5d and Extended Data Fig. 6g) also showed no abnormal or pathological signs in the heart, spleen, lung, liver or kidney after continuous inhalation of Bip-FK9.

First, we evaluated the stability of Bip-FK9 in mouse lung tissue and mouse plasma, respectively (Fig. 5e and Extended Data Fig. 6h). At 0.5 h post-administration, approximately 82.37% of the Bip-FK9 was detected in the lungs. Even at 8 h after administration, 15.01% of Bip-FK9 remained in the lung tissue. At 1 h after Bip-FK9 was added to the plasma, approximately 87.77% of the Bip-FK9 was detected. Even at 8 h after the addition of Bip-FK9, 41.30% of Bip-FK9 remained in the plasma. These results indicated that Bip-FK9 had good stability in mouse lung tissue and mouse plasma. To investigate the distribution of Bip-FK9 in mouse lungs, Cy5.5 (Cyanine-5.5) labelled Bip-FK9 (Bip-FK9-Cy5.5) was administered to the lung by nebulization for 15 min. The results indicated that Bip-FK9-Cy5.5 specifically accumulated in lung tissue for 1 h (Fig. 5f and Extended Data Fig. 6i). At 4 h after the nebulization, the red fluorescence of Bip-FK9-Cy5.5 in the lung was still observed, indicating that the residence time of Bip-FK9 in the lung was sufficient to kill bacteria. CLSM images of the lung tissue (Fig. 5g) showed that the Bip-FK9-Cy5.5 accumulated on airway epithelium and alveolar epithelium for at least 1 h after inhalation. Together, these results suggested that Bip-FK9 had good biocompatibility, good stability and long residence in lung tissue, ensuring its further antibacterial activity without side effects.

In vivo anti-infective activity of Bip-FK9 on lethal MRSA infective model

To investigate the in vivo antibacterial activity of Bip-FK9, we established a mouse model with lethal pneumonia infection and treated these mice with the peptides through nebulization[54]. Before this experiment, we assessed the antibacterial activity of Bip-FK9 in artificial mucus in vitro and examined the morphology of nebulized Bip-FK9 (Extended Data Fig. 7a,b). Compared with the control group, the concentration of MRSA in the Bip-FK9 group was reduced by approximately 10,000 times, indicating that Bip-FK9 maintained strong antibacterial efficacy in artificial mucus. In addition, the Cryo-EM image revealed that Bip-FK9 retained its nanofibre morphology after nebulization. Figure 5h,i illustrates the processes of MRSA-induced pneumonia and the treatment with Bip-FK9. To evaluate the ability of Bip-FK9 to clear MRSA from mouse lungs, lung tissues were collected from the 0.9% saline, Bip-FF, K7, Van and Bip-FK9 groups on days 2, 4, and 6. The tissues were placed into 5 ml EP tubes containing 2 ml of 0.9% saline. Following homogenization, the diluted suspensions from each group were spread onto Luria-Bertani (LB) agar plates (Fig. 5j and Supplementary Figs. 4 and 5). On day 2, the number of MRSA in the Bip-FK9 treatment group was approximately 1,600 times lower than that in the normal saline group, and roughly 50 times lower than that in the Van treatment group. By day 4, MRSA levels in the Bip-FK9 group decreased to the detection

Fig. 5 | Biosafety evaluation of Bip-FK9 in vivo and anti-infective activity of Bip-FK9 on lethal MRSA infective model in vivo. a, Body weight changes of mice that received nebulization of Bip-FK9 twice daily for 7 consecutive days. Individual data are presented as mean ± s.d. (n = 6). **b**,**c**, Th1 (**b**) and Th2 (**c**) cytokines profile in the BALF from the healthy mice and the mice that received 7-day consecutive Bip-FK9 nebulization. Individual data are presented as mean ± s.d. ($n = 6$). **d**, Representative H&E images of lung after treatment with Bip-FK9. Scale bar, 100 μm. **e**, The stability of Bip-FK9 in mouse lung tissue. Individual data are presented as mean ± s.d. ($n = 5$). **f**, Distribution of fluorescent Bip-FK9-Cy5.5 in different organs after nebulization for 1 h or 4 h ($n = 4$). From top to bottom: liver, spleen, heart, kidney and lung. **g**, Representative laser confocal scanning microscope images demonstrating pulmonary distribution mediated by Bip-FK9 labelled Cy-5.5 (red). Nuclei were stained with DAPI (blue). Scale bar, 100 μm. **h**, Schematic illustration of the nebulization therapy to treat MRSA-infected pneumonia. **i**, Timeline for antibacterial activity of peptides in the mouse model. **j**, The MRSA concentration in the lung tissues of the infected mice on day 2, day 4 and day 6, respectively. Individual data are presented as mean ± s.d. ($n = 5$). **k**, The survival curves of mice bearing pneumonia treated with Bip-FK9 or others. The 0.9% saline group ($n = 10$), the Bip-FF group ($n = 11$), the K7 group ($n = 12$), the Van group ($n = 13$) and the Bip-FK9 group ($n = 12$). **l**, H&E images of the mouse lungs to show the repair and deterioration of lung tissue over time ($n = 9$, representative images are shown). The healthy group, the 0.9% saline group on day 2 and day 4, the Van group on day 10 and the Bip-FK9 on day 10 are shown here. Scale bar, 100 μm. Scale bar in the magnified view, 40 μm. **m**, Mean linear intercept quantification of the H&E images of the mouse lungs in the healthy group, the Van group on day 10 and the Bip-FK9 group on day 10. Each dot represents data from one 10× field. Individual data are presented as mean ± s.d. ($n = 15$). **n**, Quantification of CD68 positive macrophages from lung sections. The numbers of positive cells in alveolar sites were quantified from 9 randomly chosen areas (10× field) per section using the software QuPath v0.2.0. At least one section per lung. Individual data are presented as mean ± s.d. ($n = 3$). Statistical analysis in **b**, **c**, **m** and **n** was performed using a two-tailed Student's *t*-test. Statistical analysis in **j** was performed using the Mann–Whitney test.

https://doi.org/10.1038/s41551-026-01680-0

limit, whereas approximately 10,000 CFU ml^{-1} of MRSA remained in Van treatment groups. The survival rate of mice treated with Bip-FK9 was 84% on day 10, whereas all mice treated with 0.9% saline and K7 had died by the same time point (Fig. 5k). In comparison, 46% of those in the Van treatment group remained alive on day 10. These results suggested that Bip-FK9 can eliminate MRSA in mouse lungs and reduce the degree of infection in treating fatal pneumonia.

Histopathological observation showed that a substantial number of inflammatory cells infiltrated the alveoli of the saline group (Fig. 5l and Extended Data Fig. 7c). The alveoli in the saline group began to fuse,

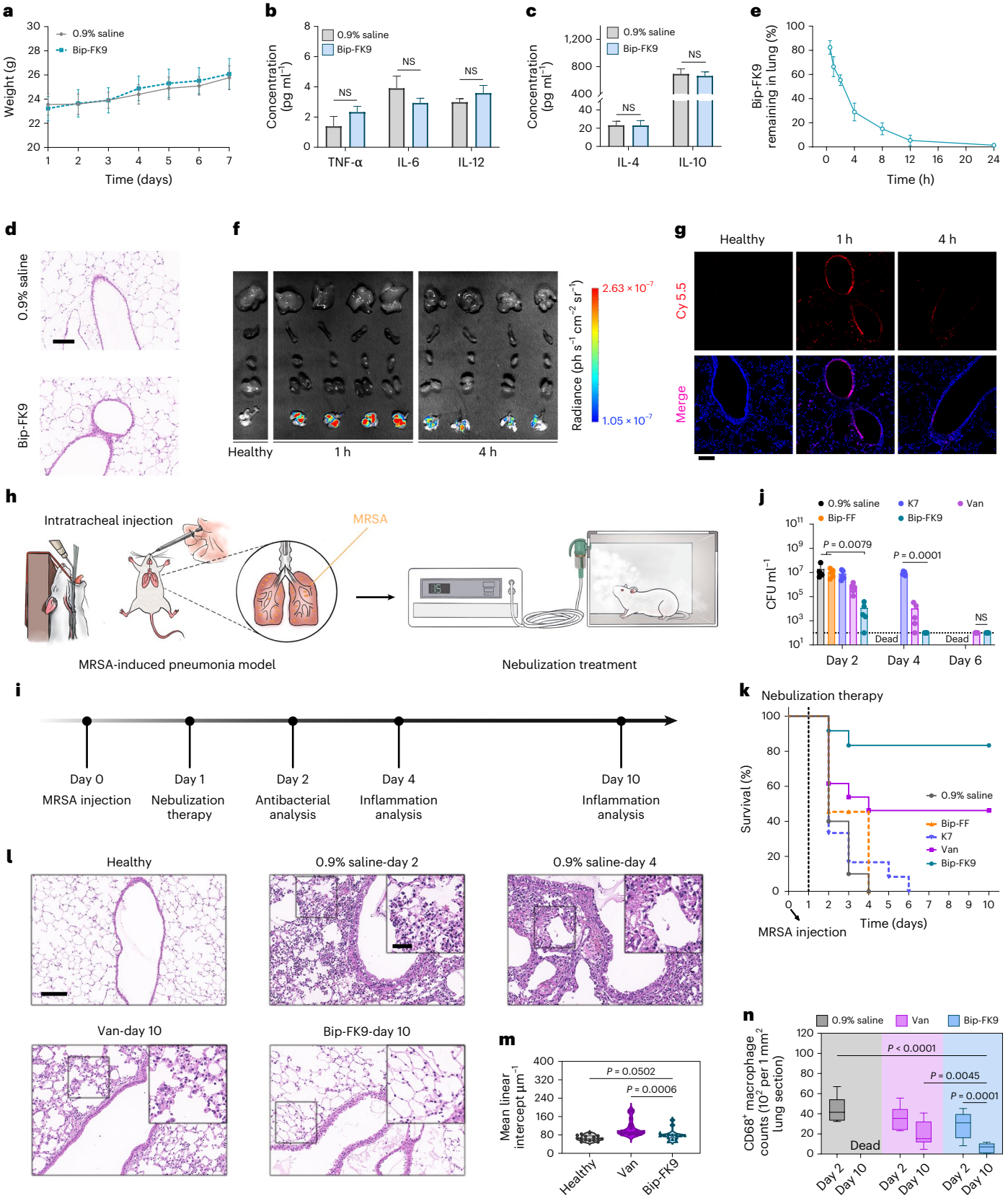

https://doi.org/10.1038/s41551-026-01680-0

Table 1 | The antimicrobial activities of peptides designed based on this work principles

Sequence	*S. aureus* USA 300	*S. aureus* ATCC 43300	*S. epidermidis* ATCC 12228	*E. coli* ATCC 25922	*E. coli* BNCC 186732	*P. aeruginosa* ATCC 27835	*K. pneumoniae* ATCC 13883	*E. cancerogenus* ATCC 35317	*S. typhimurium* BNCC 1344	*E. faecalis* ATCC 29212
KIKKWLK	>512	>512	>512	>512	>512	>512	>512	>512	>512	>512
Bip-FFKIKKWLK	8	8	8	16	16	8	64	32	8	32
KWKLFKK	>512	>512	>512	>512	>512	>512	>512	>512	>512	>512
Bip-FFKWKLFKK	8	32	128	8	16	32	128	32	32	32
LKRVWKR	>512	>512	>512	>512	>512	>512	>512	>512	>512	>512
Bip-FFLKRVWKR	32	16	16	16	16	64	32	32	128	128
RLKKWIQ	>512	>512	>512	>512	>512	>512	>512	>512	>512	>512
Bip-FFRLKKWIQ	32	32	8	32	32	64	>128	32	32	32
KLLKRYWR	>128	>128	>512	256	>128	256	>512	>512	256	>512
Bip-FFKLLKRYWR	8	8	4	8	8	16	16	8	8	16

The MIC (μM) values of these peptides against the different strains, including *Staphylococcus aureus* (*S. aureus*), *Staphylococcus epidermidis* (*S. epidermidis*), *Escherichia coli* (*E. coli*), *Pseudomonas aeruginosa* (*P. aeruginosa*), *Enterobacter cancerogenus* (*E. cancerogenus*), *Klebsiella pneumoniae* (*K. pneumoniae*), *Salmonella typhimurium* (*S. typhimurium*) and *Enterococcus faecalis* (*E. faecalis*) strain.

and the tracheal wall began to thicken on day 2. On day 4, there were almost no intact alveoli in the lung tissue of the mice, and the immune cells filled in the alveoli, eventually leading to the death of mice in the saline group. By contrast, the lungs of mice treated with Bip-FK9 appeared to have few inflammatory cells infiltrating the alveoli on day 4, indicating that the lung tissue was beginning to recover. On day 10, the Van group exhibited a slightly higher number of inflammatory cells in the lung stroma compared with the healthy group and the Bip-FK9 group. By contrast, the Bip-FK9 group showed lung inflammatory cell levels comparable to those of the healthy group. The pulmonary mean linear intercept in the Bip-FK9 group was comparable to that of the healthy group (Fig. 5m). These findings indicated that the degree of recovery in mice treated with Bip-FK9 was greater than that observed in the Van group. To further evaluate the difference in the degree of lung recovery between the antibiotic (Van) and the Bip-FK9 groups, we labelled macrophages in lungs with CD68 antibody (Fig. 5n and Supplementary Fig. 6) and performed a quantitative analysis. For the Bip-FK9 group, we compared the infiltration of macrophages in lung tissue on different days. We found a substantial decrease in lung macrophages on day 10 of Bip-FK9 treatment compared with that on day 2 ($P = 0.0001$, $n = 3$). Compared with the Van group on day 10, the lung macrophages in the Bip-FK9 group were fewer on day 10 ($P = 0.0045$, $n = 3$). These results indicated that Bip-FK9 treatment enabled lung function in mice to return to normal levels rapidly.

Conclusion

By rationally designing the antimicrobial consisting of a membrane-anchor motif, a self-assembly linker and a cationic minimalistic peptide truncated from the natural reservoir, we demonstrated the universality of the design principles and verified its activity against a broad spectrum of bacteria (Table 1).

We report an antimicrobial, Bip-FK9, for combating multidrug-resistant bacteria without inducing acquired drug resistance. Cryo-EM and MD simulations revealed the formation of nanofibres on the cell surface to induce bacterial death. Haemolysis and in vivo biosafety experiments suggested that Bip-FK9 had a large therapeutic window to protect against bacterial infections. Moreover, the designed peptide in this work exhibited excellent antibacterial efficiency and improved mouse survival rates after MRSA-induced lung infection in a mouse model without causing notable toxicity to major organs. We acknowledge that the cell wall barrier of MRSA partially hinders Bip-FK9 from binding to PG on the bacterial membrane, thereby reducing its antibacterial activity to some extent. Nevertheless, this study, including in vitro and in vivo antibacterial experiments as well as biosafety assessments, demonstrates that Bip-FK9 still remains a promising candidate as an effective antibacterial agent. Bip-FK9 shows promise in killing bacterial populations, making it a candidate for treating conditions such as suppurative arthritis, acute pneumonia and intervertebral infections.

Methods

Materials

NPN, Cip, 3,3-dipropylthiadicarbocyanine iodide $DiSC_3(5)$, trifluoroacetic acid (TFA), 1,2-distearoyl-sn-glycero-3-phosphate (sodium salt) (PA), CL and Van were bought from Aladdin. Rhodamine 6G and diethylenetriamine pentaacetic acid (DTPA) were purchased from Macklin. 1,2-Dioleoyl-sn-glycero-3-phosphocholine (PC), 1,2-dioleoyl-sn-glycero-3-phospho-(1′-rac-glycerol) (PG), sphingomyelin (SM), cholesterol (Cho), 1,2-dipalmitoyl-sn-glycero-3-phospho-L-serine (PS) and 1,2-distearoyl-sn-glycero-3-phosphoethanolamine (PE) were obtained from AVT (Shanghai) Pharmaceutical Tech. Mucin was purchased from Leyan. *N*,*N*-diisopropylethylamine (DIPEA), LTA, PepGly and 1,2-dioleoyl-sn-glycero-3-[phospho-rac-(3-lysyl(1-glycerol))] (Lysyl-PG) were obtained from Merck KGaA. Phosphatidylinositol (PI) was purchased from Beijing Unique Biotechnology. Amino acids protected by Fmoc and *O*-(7-azabenzotriazol-1-yl)-*N*,*N*,*N*′,*N*′-tetramethyluronium hexafluophosphate (HBTU) were purchased from GL Biochem. 2-Chlorotrityl chloride resin was provided by Tianjin Nankai Hecheng Sci&Tech. 3-Chlorophenylacetic acid (Chl), 4-biphenylacetic acid (Bip), 2-naphthaleneacetic acid (Nap), 1-adamantaneacetic acid (Ada), *n*-octanoic acid (Oct) and 2-(4-isopropylphenyl)acetic acid (Iso) were bought from Aladdin. Peptides were synthesized by standard solid-phase peptide synthesis (SPPS)[55,56]. Magainin II (GIGKFLHSAKKFGKAFVGEIMNS), Melittin (GIGAVLKVLTTGLPALISWIKRKRQQ) and Ovispirin (KNLRRIIRKIIHIIKKYG) were purchased from the GL Biochem. Pexiganan acetate (GIGKFLKKAKKFGKAFVKILKK), Omiganan (ILRWPWWPWRRK), OP-145 (IGKEFKRIVERIKRFLRELVRPLR) and Ghrelin (GSSFLSPEHQRVQQRKESKKPPAKLQPR) were purchased from the Nanjing TGpeptide.

Cryo-EM experiments of Bip-FK9

The morphology of the peptide was observed by Cryo-EM (CRYO-EM001, Thermo Fisher). The Bip-FK9 (128 μM), K7 (128 μM) and Bip-FF (128 μM) were prepared in PBS buffer (pH 7.4), respectively, and then rested for 12 h. Moreover, Bip-FK9 solution at a concentration of 128 μM was added to a mouse nebulizer (KW-DM-YWH, NJKEW Biotechnology). Then, the nebulized solution was collected. These solutions (5 μl) were transferred to electron microscopy grids. The grids were placed into a cryo-holder and visualized using a 200 kV Cryo-EM.

Bacterial strains

Methicillin-resistant *Staphylococcus aureus* USA 300 (MRSA), *Enterococcus faecalis* ATCC 29212, methicillin-resistant *Staphylococcus aureus* ATCC 43300, *Pseudomonas aeruginosa* ATCC 27835, *Escherichia coli* ATCC 25922 and *Klebsiella pneumoniae* ATCC 13883 were provided by Hangzhou Biosci Biotechnology. *Salmonella typhimurium* BNCC 1344, *Staphylococcus epidermidis* ATCC 12228, multidrug-resistant *Escherichia coli* BNCC 186732 and *Enterobacter cancerogenus* ATCC 35317 were purchased from Beijing Beina Chuanglian Biotechnology Institute. Here methicillin-resistant *Staphylococcus aureus* USA 300 (MRSA) was used for further analysis.

MIC and MBC determinations

According to the Clinical and Laboratory Standards Institute (CLSI) recommendations[57,58], the standard broth micro-dilution was used to determine the MICs and MBCs of peptides. In brief, 100 µl of the mid-logarithmic growth-phase bacteria at the concentration of 1×10^6 CFU ml^{-1} were added to the 96-well plates. Then, 100 µl of serial 2-fold dilution of peptides at concentrations from 1,024 µM to 1 µM was added to the 96-well plates. The plates were placed into an incubator and incubated for 20 h. After the incubation, the MICs were obtained by observing the no visible growth in wells of the lowest peptide concentration group. In addition, 10 µl of cultures from each well were spread on solid LB agar plates after the incubation. Then, the plates were incubated at 37 °C for 24 h. MBCs were determined based on the plates of the lowest peptide concentration group without bacterial colony growth. The MIC and MBC experiments were performed three times independently.

In vitro antibacterial activity experiment

A mid-logarithmic growth-phase MRSA at 5×10^6 CFU ml^{-1} was prepared in LB medium and added to a 96-well plate at 180 µl well^{-1}. Deionized water (20 µl) containing a serial concentration of Bip-FK9 (320 µM, 160 µM, 80 µM and 40 µM) was added to the 96-well plate. The Bip-FF (320 µM) and K7 (320 µM) were also added to 96-well plates in the same method. The plates were incubated at 37 °C for 24 h, and the optical density of the plate at 600 nm (OD_{600}) was measured by a Microplate Reader (Varioskan Lux, Thermo Fisher) every 2 h. At 8 h, 10 µl diluted solution from the control, Bip-FF (32 µM), K7 (32 µM) and Bip-FK9 (32 µM) groups was spread on solid LB agar plates, and then the plates were incubated at 37 °C for 24 h. The number of colony-forming units (CFU) was considered to evaluate the viability of MRSA growth. The minimum detection was set as 100 CFU ml^{-1}.

Antibacterial activity of Bip-FK9 compared with that of classical antibiotics (Van)

The stationary growth-phase MRSA at 1×10^8 CFU ml^{-1} in LB medium was added to a 96-well plate at 100 µl well^{-1}. Serial 2-fold dilution (100 µl) of Van and Bip-FK9 at concentrations from 2,048 µM to 16 µM was added to the 96-well plates. The plates were placed into an incubator and incubated for 18 h. Diluted solution (10 µl) from each group was spread on solid LB agar plates, and the plates were placed in an incubator for 24 h at 37 °C. The MRSA CFUs on the plates were counted to determine the bacterial concentration in each well.

Evaluation of the anti-biofilm ability of peptide

A mid-logarithmic growth-phase MRSA at 5×10^6 CFU ml^{-1} was prepared in LB medium and added to a 96-well plate at 200 µl well^{-1}. The plates were incubated at 37 °C for 48 h. The LB medium was changed every 12 h. After this process, the LB medium was aspirated from the 96-well plate and washed with sterile PBS three times. The 96-well plate was added 200 µl of PBS containing Bip-FF (128 µM), K7 (128 µM) or Bip-FK9 (128 µM) and co-incubated at 37 °C for 4 h, respectively. The PBS contained nothing as the control group. A 10 µl pipette tip was used to scrape off the bacteria that formed the biofilm in the 96-well plate, and the plate was put in the ultrasonic machine for more than 1 min to distribute the bacteria in the solution. The 10 µl diluted solution of different groups was spread on solid LB agar plates, respectively. After co-incubation of MRSA biofilm and the peptides, the biofilm was fixed by 2.5% glutaraldehyde for 2 h and dehydrated with gradient ethanol solutions before being measured by an analytical field emission scanning electron microscope (FE-SEM, GeminiSEM 450). After staining with a LIVE/DEAD BackLight bacterial viability kit (Invitrogen), CLSM (Zeiss LSM 800) detected the MRSA biofilm.

Resistance-acquisition experiment

Drug-resistance measurement of MRSA was tested by repeatedly treating MRSA with peptides and Cip at the sub-MIC concentration[43,59], respectively. The MIC measurement of MRSA was conducted according to instructions provided by the Clinical and Laboratory Standard Institute[9,10]. The next generation of MRSA was initiated by growing the MRSA suspension at a sub-MIC concentration, and another MIC measurement was conducted. After co-incubation for 20 h, the MRSA treated with a sub-MIC concentration of the Bip-FK9 or Cip was tested for MIC. The process will continue to reach 30 generations.

Rapid antimicrobial activity of Bip-FK9 compared with that of classical AMPs

The stationary growth-phase MRSA at 1×10^8 CFU ml^{-1} in PBS (360 µl) was added to 1.5 ml EP tubes. Deionized water (40 µl) containing Omiganan (1.28 mM), Pexiganan acetate (1.28 mM), OP-145 (1.28 mM), Ghrelin (1.28 mM), Magainin II (1.28 mM), Ovispirin (1.28 mM), Melittin (1.28 mM) and Bip-FK9 (1.28 mM) were added into the tubes, respectively. The tubes were put on a shaker at 37 °C for 2 h. At designated time points (1 min, 5 min, 10 min, 30 min, 60 min and 120 min), 10 µl diluted solution from each group was spread on solid LB agar plates, and the plates were placed in an incubator for 24 h at 37 °C. The MRSA CFUs on the plates were counted to determine the bacterial concentration in the tubes.

Cryo-EM experiments of MRSA treated with peptides (Bip-FF, K7 and Bip-FK9)

MRSA in the mid-logarithmic growth phase was washed with PBS 3 times and diluted to 1×10^8 CFU ml^{-1}. The bacterial suspension was co-cultured with the peptides for 8 h, and the final concentration of the peptide was 128 µM. During incubation, the bacterial mixtures were chosen to prepare Cryo-EM samples at 4 h and 8 h, respectively. The mixtures were fixed and transferred to electron microscopy grids. The grids were placed into a cryo-holder and visualized under a 200 kV Cryo-EM (CRYO-EM001, Thermo Fisher).

Propidium iodide (PI) staining of MRSA treated with peptides

PI, a red fluorescent dye that cannot penetrate intact cell membranes, can enter cells when their membrane is damaged, and stained them. MRSA in the mid-logarithmic growth phase was washed with PBS 3 times and diluted to 1×10^8 CFU ml^{-1}. The bacterial suspension was co-cultured with Bip-FF, K7 and Bip-FK9 for 4 h and 8 h, respectively, and the final concentration of the peptides was 128 µM. Moreover, 1% Triton X-100 was added to the bacterial suspension as the positive control. After the incubation, the PI dye was added to the bacterial suspension at the concentration of 2 µg ml^{-1}. After the 20 min incubation, the PBS was used to wash the bacteria three times. Finally, the bacterial suspension was transferred to 96-well plates. The fluorescence intensity of PI (excitation wavelength (Ex), 535 nm; emission wavelength (Em), 620 nm) in each well was recorded using a microplate reader (Spark, Tecan).

Intracellular ATP level evaluation

The ATP level in bacteria was determined by the ATP Assay Kit (Beyotime, catalogue number S0026). After MRSA was grown in the fresh LB media overnight, we used PBS to wash MRSA 3 times and diluted

it to a final concentration of 2×10^8 CFU ml^{-1}. MRSA suspension (100 µl) was added to a 96-well plate including 100 µl peptides (256 µM) and co-incubated for 4 h. The mixture was washed with PBS three times. ATP levels in bacteria were measured according to the manufacturer's instructions.

Dissociation constant measurement

The binding affinity of Bip-FK9 to PG and PS was evaluated by ITC (MicroCal PEAQ-ITC, Malvern Panalytical Limited), respectively. First, the lipids were made into liposomes using the extrusion techniques as previously reported. In brief, PS and PG were dissolved in chloroform (the total lipid concentration, 5 mM), respectively, and dried by N_2 flows, followed by overnight lyophilization. The dry film was resuspended using HEPES (10 mM, pH 7.4) and homogenized through ultrasonication (15 min) to allow even dispersion. Subsequently, the suspension was extruded through a 0.1 µm pore polycarbonate membrane using an Avanti Mini Extruder (Alabaster) more than 20 times. Bip-FK9 was dissolved in HEPES buffer (10 mM, pH 7.4) at a concentration of 50 µM, and PG was diluted in HEPES (10 mM, pH 7.4) to reach a concentration of 500 µM. Continuous injections of PG into the calorimetric cell filled with Bip-FK9 were repeated 19 times (equilibration intervals were 180 s). MicoCal PEAQ-ITC Analysis Software calculated thermodynamic parameters: the equilibrium dissociation constant (K_D) = 84.9 nM. Moreover, Bip-FK9 was dissolved in HEPES buffer (10 mM, pH 7.4) at the concentration of 100 µM, and PS was diluted in HEPES (10 mM, pH 7.4) to reach a concentration of 500 µM. Continuous injections of PS into the calorimetric cell filled with Bip-FK9 were repeated 19 times (equilibration intervals were 180 s). MicoCal PEAQ-ITC Analysis Software calculated thermodynamic parameters: the equilibrium dissociation constant (K_D) = 415 nM.

NMR experiments

PG was dissolved in chloroform and dried by N_2 flows, followed by overnight lyophilization. The dry film was resuspended using HEPES (10 mM, D_2O). It was homogenated using an ultrasonic homogenizer (JY92-IIN, Ningbo Scientz Biotechnology) for 10 min under the power of 150 W to obtain a clear solution (2.56 mM). Bip-FK9 was dissolved in HEPES (10 mM, D_2O) at a concentration of 2.56 mM. All spectra of the BipF-FK9 blended with PG were measured using a 600 MHz solution NMR spectrometer with cryo-probe (AVANCE NEO, Bruker BioSpin). For the ^{19}F spectra, the ^{1}H-decoupled ^{19}F spectra were recorded with 128 k data points, 1 s relaxation delay and 256 scans using the 'zgig' pulse sequence. Longitudinal relaxation time constants (T1) of ^{19}F were measured using the standard 't1ir' inversion recovery pulse sequence with 16 delay times ranging from 0.0005 s to 16.384 s. Transverse relaxation time constants (T2) of ^{19}F were measured using the conventional 'cpmg' pulse sequence with a relaxation delay value of 7.5 s, an echo delay (τ) of 0.5 ms and 12 loop counter values varying from 5 to 10,000. Two-dimensional ^{1}H–^{1}H NOESY experiments were obtained by the 'noesyphpr' pulse sequence with 150 ms mixing time. These 2D data were collected with 96 scans, 2,048 data points in the direct dimension and 256 increments in the indirect dimension. A relaxation delay of 1.5 s was used.

Cytocompatibility assay

About 10^4 human alveolar basal epithelial cells (A549) and mouse macrophages (RAW 264.7) were seeded in 96-well plates and incubated for 24 h, respectively. After discarding the medium, fresh medium containing different samples (128 µM) was added to the plates. After incubating for 72 h, we used an MTT assay to measure the cell viability.

TEM images of A549 cells under the treatment of Bip-FK9

First, A549 cells (1×10^6) were seeded in 6-well plates and incubated for 24 h at 37 °C in a humidified atmosphere of 5% CO_2. After incubation, the old medium was removed. The fresh medium containing Bip-FK9 (128 µM) was added to the plates, respectively, and incubated for 4 h. The plates were washed with PBS three times. PBS (900 µl) mixed with 100 µl of fetal bovine serum (FBS), which was added to the plates. Then, the A549 cells attached to the plates were gently scraped off and centrifuged. The supernatant was removed, and 2.5% glutaraldehyde was added to the plates. The cell suspension was transferred to 1.5 ml EP tubes. Under the guidelines of the Westlake Electron Microscopy Core Facility, the A549 cells were embedded and stained. A transmission electron microscope (Talos L120C G2) was used to observe the morphology of the treated cells.

Animals

All the animal experiments were performed under the guidelines of the Institutional Animal Care and Use Committee (IACUC) and the Westlake University Animal Care and Use Protocol (number 21-046-WHM) at Westlake University. Eight-week-old male BALB/c mice were purchased from Shanghai Slake Experimental Animal.

Biosafety evaluation in mice

To evaluate the potential pulmonary side effects caused by the Bip-FK9 local treatment, 12 mice were randomly divided into 2 groups ($n = 6$), then subjected to nebulization (twice a day) with 0.9% saline or Bip-FK9 (128 µM in 0.9% saline) for consecutive 7 days. The body weight was monitored daily. The BALF was extracted for cytokines analysis and leukocyte differentiation after 7 days of consecutive nebulization. The serum was collected from these mice. The specific mice enzyme-linked immunosorbent assay (ELISA) kits (Bioswamp) were used to determine the concentration of IgG and IgE in the collected serum. The lung was injected with 2 ml warm 1% agarose solution through the trachea, embedded in paraffin and then subjected to histological staining with H&E.

In vivo Bip-FK9 stability in mouse lungs

The healthy mice were anaesthetized by intraperitoneal injection of 2.5% Avertin (18–20 µl g^{-1}) and immobilized on a surgery board tilted at 60 degrees. The oropharyngeal structures were magnified and illuminated by a laryngoscope purchased from Welch Allyn. A mouse-trachea-sized sterile polyethylene tube was guided by a laryngoscope and inserted into the mouse trachea. Then, a dose of Bip-FK9 (50 µl, 128 µM) was delivered to the lungs through intratracheal instillation. At designated time points (30 min, 1 h, 2 h, 4 h, 8 h, 12 h and 24 h), the mice ($n = 5$) from each group were killed and their major organs were removed. Then, after cardiac perfusion with 10 ml of cold PBS, mouse lung tissues were collected and lyophilized. The tissues were crushed into powder and weighed. The solution consisting of methanol/chloroform (volume ratio = 3:1) was used to resuspend the tissue powder. A bullet blender (JXFSTPRP-II, Shanghai Jinxin) was used to grind the suspension with the help of steel grinding beads (⌀3.2 mm and ⌀5.2 mm). Next, the homogenized lung tissues were centrifuged (15,000 r.p.m., 5 min), and the supernatant was collected, followed by filtering by 0.22 µm filters. An Agilent 1260 Infinity Lab Liquid Chromatography system with an Infinity Lab Poroshell 120 EC-C18 column (4.5 × 50 mm, 2.7 µm, #699975-902, Agilent Technologies) was used to analyse the Bip-FK9 content in the supernatant.

Bip-FK9 stability in mouse plasma

Blood was collected from healthy mice using the posterior orbital venous plexus sampling method, and the collected blood was transferred to an anticoagulant tube containing heparin. The anticoagulant tube was centrifuged (5,000 r.p.m., 10 min), and the supernatant was collected. Next, the Bip-FK9 solution and the plasma were pre-warmed at 37 °C for 10 min. Plasma (180 µl) was added into 1.5 ml EP tubes containing 20 µl of Bip-FK9 solution (1.28 mM). At designated time points (1 h, 2 h, 4 h, 8 h, 12 h and 24 h), 200 µl of stop solution (MeOH/ACN = 1:1) was added to the EP tubes to stop the reaction. Next, the tubes were

centrifuged (15,000 r.p.m., 5 min), and the supernatant was collected, followed by filtering by 0.22 μm filters. An Agilent 1260 Infinity Lab Liquid Chromatography system with an Infinity Lab Poroshell 120 EC-C18 column (4.5 × 50 mm, 2.7 μm, #699975-902, Agilent Technologies) was used to analyse the Bip-FK9 content in the supernatant.

Mouse infection model

To create a mouse model of bacterial pneumonia, the bacteria were administrated to mice through intratracheal injection. First, the MRSA was seeded into LB media and grown for 10 h. The cultures were centrifuged (7,500 r.p.m., 10 min) and washed three times with sterile phosphate-buffered saline (PBS). In brief, the mice were anaesthetized by intraperitoneal injection of 2.5% Avertin (18–20 μl g^{-1}) and immobilized on a surgery board tilted at 60 degrees. The oropharyngeal structures were magnified and illuminated by a laryngoscope purchased from Welch Allyn. A mouse-trachea-sized sterile polyethylene tube was guided by a laryngoscope and inserted into the mouse trachea. Then, a lethal dose of MRSA (1×10^8 CFU) was delivered to the lungs through intratracheal instillation. After 24 h of infection with MRSA, mice were administrated with Bip-FF ($n = 11$), K7 ($n = 12$) and Bip-FK9 ($n = 12$) at a concentration of 128 μM via a mouse nebulizer (KW-DM-YWH, NJKEW Biotechnology). Saline (0.9%) ($n = 10$) was chosen as a control in nebulization. Moreover, the mice in the Van group ($n = 12$) received two times dosing of Van at a dosage of 10 mg kg^{-1} through intravenous injection at 24 h and 96 h post-infection, respectively. All the mice were observed to evaluate their health status for 10 days.

In vivo antibacterial assay

On day 2, day 4 and day 6, the lungs of mice from the 0.9% saline, Bip-FF, K7, Van and Bip-FK9 groups were collected and placed into 5 ml EP tubes containing 2 ml of 0.9% saline. Following homogenization, 10 μl diluted solution of each group was spread on solid LB agar plates, and the plates were placed in an incubator for 24 h at 37 °C.

Statistics and reproducibility

The data were processed based on GraphPad Prism 9 software, using a one-way classification of analysis of variance (ANOVA) and two-tailed heteroscedastic Student's *t*-test. Differences were regarded as statistically significant, while $P < 0.05$. All experiments were repeated at least three times with similar results.

Reporting summary

Further information on research design is available in the Nature Portfolio Reporting Summary linked to this article.

Data availability

All data that support the findings of this study are available within the paper and the Supplementary Files, or from the authors upon request. Source data are provided with this paper.

References

1. Ventola, C. L. The antibiotic resistance crisis: part 1: causes and threats. *Pharm. Ther.* **40**, 277 (2015).
2. Byrne, M. K. et al. The drivers of antibiotic use and misuse: the development and investigation of a theory driven community measure. *BMC Public Health* **19**, 1–11 (2019).
3. *WHO Report on Surveillance of Antibiotic Consumption: 2016-2018 Early Implementation* (World Health Organization, 2018).
4. Fjell, C. D., Hiss, J. A., Hancock, R. E. & Schneider, G. Designing antimicrobial peptides: form follows function. *Nat. Rev. Drug Discov.* **11**, 37–51 (2012).
5. Frei, A., Verderosa, A. D., Elliott, A. G., Zuegg, J. & Blaskovich, M. A. Metals to combat antimicrobial resistance. *Nat. Rev. Chem.* **7**, 202–224 (2023).
6. Stabryla, L. M. et al. Role of bacterial motility in differential resistance mechanisms of silver nanoparticles and silver ions. *Nat. Nanotechnol.* **16**, 996–1003 (2021).
7. Linklater, D. P. et al. Mechano-bactericidal actions of nanostructured surfaces. *Nat. Rev. Microbiol.* **19**, 8–22 (2021).
8. Harms, A., Maisonneuve, E. & Gerdes, K. Mechanisms of bacterial persistence during stress and antibiotic exposure. *Science* **354**, aaf4268 (2016).
9. Mourtada, R. et al. Design of stapled antimicrobial peptides that are stable, nontoxic and kill antibiotic-resistant bacteria in mice. *Nat. Biotechnol.* **37**, 1186–1197 (2019).
10. Blair, J., Webber, M. A., Baylay, A. J., Ogbolu, D. O. & Piddock, L. J. Molecular mechanisms of antibiotic resistance. *Nat. Rev. Microbiol.* **13**, 42–51 (2015).
11. de Breij, A. et al. The antimicrobial peptide SAAP-148 combats drug-resistant bacteria and biofilms. *Sci. Transl. Med.* **10**, eaan4044 (2018).
12. Puthia, M. et al. A dual-action peptide-containing hydrogel targets wound infection and inflammation. *Sci. Transl. Med.* **12**, eaax6601 (2020).
13. Hancock, R. E., Alford, M. A. & Haney, E. F. Antibiofilm activity of host defence peptides: complexity provides opportunities. *Nat. Rev. Microbiol.* **19**, 786–797 (2021).
14. Dijksteel, G., Ulrich, M., Middelkoop, E. & Boekema, B. Review: lessons learned from clinical trials using antimicrobial peptides (AMPs). *Front. Microbiol.* **12**, 616979 (2021).
15. Nederberg, F. et al. Biodegradable nanostructures with selective lysis of microbial membranes. *Nat. Chem.* **3**, 409–414 (2011).
16. Hancock, R. E. & Sahl, H.-G. Antimicrobial and host-defense peptides as new anti-infective therapeutic strategies. *Nat. Biotechnol.* **24**, 1551–1557 (2006).
17. Fernandez-Lopez, S. et al. Antibacterial agents based on the cyclic D,L-α-peptide architecture. *Nature* **412**, 452–455 (2001).
18. Si, Z. et al. A glycosylated cationic block poly(β-peptide) reverses intrinsic antibiotic resistance in all ESKAPE Gram-negative bacteria. *Angew. Chem. Int. Ed.* **59**, 6819–6826 (2020).
19. Sloand, J. N., Miller, M. A. & Medina, S. H. Fluorinated peptide biomaterials. *Pept. Sci.* **113**, e24184 (2021).
20. Zhong, C. et al. Antimicrobial peptides conjugated with fatty acids on the side chain of D-amino acid promises antimicrobial potency against multidrug-resistant bacteria. *Eur. J. Pharm. Sci.* **141**, 105123 (2020).
21. Mitra, S. et al. Cyclization of two antimicrobial peptides improves their activity. *ACS Omega* **10**, 9728–9740 (2025).
22. White, J. K. et al. A synthetic cyclized antimicrobial peptide with potent effects against drug-resistant skin pathogens. *ACS Infect. Dis.* **9**, 1056–1063 (2023).
23. Laverty, G., McLaughlin, M., Shaw, C., Gorman, S. P. & Gilmore, B. F. Antimicrobial activity of short, synthetic cationic lipopeptides. *Chem. Biol. Drug Des.* **75**, 563–569 (2010).
24. Strandberg, E. et al. Influence of hydrophobic residues on the activity of the antimicrobial peptide magainin 2 and its synergy with PGLa. *J. Pept. Sci.* **21**, 436–445 (2015).
25. Lam, S. J. et al. Combating multidrug-resistant Gram-negative bacteria with structurally nanoengineered antimicrobial peptide polymers. *Nat. Microbiol.* **1**, 1–11 (2016).
26. Blaskovich, M. A. et al. A lipoglycopeptide antibiotic for Gram-positive biofilm-related infections. *Sci. Transl. Med.* **14**, eabj2381 (2022).
27. Liu, L. et al. Self-assembled cationic peptide nanoparticles as an efficient antimicrobial agent. *Nat. Nanotechnol.* **4**, 457–463 (2009).
28. Levin, A. et al. Biomimetic peptide self-assembly for functional materials. *Nat. Rev. Chem.* **4**, 615–634 (2020).

29. Pappas, C. G. et al. Dynamic peptide libraries for the discovery of supramolecular nanomaterials. *Nat. Nanotechnol.* **11**, 960–967 (2016).
30. Smith, D. J. et al. A multiphase transitioning peptide hydrogel for suturing ultrasmall vessels. *Nat. Nanotechnol.* **11**, 95–102 (2016).
31. Álvarez, Z. et al. Bioactive scaffolds with enhanced supramolecular motion promote recovery from spinal cord injury. *Science* **374**, 848–856 (2021).
32. Wang, H., Feng, Z. & Xu, B. Assemblies of peptides in a complex environment and their applications. *Angew. Chem. Int. Ed.* **131**, 10532–10541 (2019).
33. Shigemitsu, H. et al. An adaptive supramolecular hydrogel comprising self-sorting double nanofibre networks. *Nat. Nanotechnol.* **13**, 165–172 (2018).
34. Wu, D. et al. Polymers with controlled assembly and rigidity made with click-functional peptide bundles. *Nature* **574**, 658–662 (2019).
35. Mookherjee, N., Anderson, M. A., Haagsman, H. P. & Davidson, D. J. Antimicrobial host defence peptides: functions and clinical potential. *Nat. Rev. Drug Discov.* **19**, 311–332 (2020).
36. Wang, G., Li, X. & Wang, Z. APD3: the antimicrobial peptide database as a tool for research and education. *Nucleic Acids Res.* **44**, D1087–D1093 (2016).
37. Costa, F., Teixeira, C., Gomes, P. & Martins, M. C. L. Clinical application of AMPs. *Adv. Exp. Med. Biol.* **1117**, 281–298 (2019).
38. Kim, W. et al. A new class of synthetic retinoid antibiotics effective against bacterial persisters. *Nature* **556**, 103–107 (2018).
39. Martin II, J. K. et al. A dual-mechanism antibiotic kills Gram-negative bacteria and avoids drug resistance. *Cell* **181**, 1518–1532.e1514 (2020).
40. Wang, M. et al. Modular design of membrane-active antibiotics: from macromolecular antimicrobials to small scorpionlike peptidomimetics. *J. Med. Chem.* **64**, 9894–9905 (2021).
41. Wang, J. et al. Intracellular condensates of oligopeptide for targeting lysosome and addressing multiple drug resistance of cancer. *Adv. Mater.* **34**, 2104704 (2022).
42. Torres, M. D., Melo, M. C., Crescenzi, O., Notomista, E. & de la Fuente-Nunez, C. Mining for encrypted peptide antibiotics in the human proteome. *Nat. Biomed. Eng.* **6**, 67–75 (2022).
43. Das, P. et al. Accelerated antimicrobial discovery via deep generative models and molecular dynamics simulations. *Nat. Biomed. Eng.* **5**, 613–623 (2021).
44. Kim, W. et al. A selective membrane-targeting repurposed antibiotic with activity against persistent methicillin-resistant *Staphylococcus aureus*. *Proc. Natl Acad. Sci. USA* **116**, 16529–16534 (2019).
45. Song, M. et al. A broad-spectrum antibiotic adjuvant reverses multidrug-resistant Gram-negative pathogens. *Nat. Microbiol.* **5**, 1040–1050 (2020).
46. Chen, Y.-F., Sun, T.-L., Sun, Y. & Huang, H. W. Interaction of daptomycin with lipid bilayers: a lipid extracting effect. *Biochemistry* **53**, 5384–5392 (2014).
47. PináChen, Y. Bio-inspired resin acid-derived materials as anti-bacterial resistance agents with unexpected activities. *Chem. Sci.* **5**, 2011–2016 (2014).
48. Chen, E. H.-L. et al. Visualizing the membrane disruption action of antimicrobial peptides by cryo-electron tomography. *Nat. Commun.* **14**, 5464 (2023).
49. De Kimpe, S. J., Kengatharan, M., Thiemermann, C. & Vane, J. R. The cell wall components peptidoglycan and lipoteichoic acid from *Staphylococcus aureus* act in synergy to cause shock and multiple organ failure. *Proc. Natl Acad. Sci. USA* **92**, 10359–10363 (1995).
50. Hayami, M., Okabe, A., Kariyama, R., Abe, M. & Kanemasa, Y. Lipid composition of *Staphylococcus aureus* and its derived L-forms. *Microbiol. Immunol.* **23**, 435–442 (1979).
51. Simonson, A. W. et al. Pathogen-specific antimicrobials engineered de novo through membrane-protein biomimicry. *Nat. Biomed. Eng.* **5**, 467–480 (2021).
52. Zambrano, F., Fleischer, S. & Fleischer, B. Lipid composition of the Golgi apparatus of rat kidney and liver in comparison with other subcellular organelles. *Biochim. Biophys. Acta* **380**, 357–369 (1975).
53. Leventis, P. A. & Grinstein, S. The distribution and function of phosphatidylserine in cellular membranes. *Annu. Rev. Biophys.* **39**, 407–427 (2010).
54. Zhou, Z. et al. Using tea nanoclusters as β-lactamase inhibitors to cure multidrug-resistant bacterial pneumonia: a promising therapeutic strategy by Chinese materioherbology. *Fundam. Res.* **2**, 496–504 (2022).
55. Yang, X., Lu, H., Tao, Y., Zhou, L. & Wang, H. Spatiotemporal control over chemical assembly in living cells by integration of acid-catalyzed hydrolysis and enzymatic reactions. *Angew. Chem. Int. Ed.* **60**, 23797–23804 (2021).
56. Hu, L. et al. Structure-based programming of supramolecular assemblies in living cells for selective cancer cell inhibition. *Angew. Chem. Int. Ed.* **60**, 21807–21816 (2021).
57. *Methods for Dilution Antimicrobial Susceptibility Tests for Bacteria That Grow Aerobically* CLSI Approved Standard—Seventh Edition CLSI Document M7-A72006 (Clinical and Laboratory Standards Institute, 2006).
58. Barry, L. A. et al. *Methods for Determining Bactericidal Activity of Antimicrobial Agents: Approved Guideline* Vol. 19 (National Committee for Clinical Laboratory Standards, 1999).
59. Friedman, L., Alder, J. D. & Silverman, J. A. Genetic changes that correlate with reduced susceptibility to daptomycin in *Staphylococcus aureus*. *Antimicrob. Agents Chemother.* **50**, 2137–2145 (2006).

Acknowledgements

This project was supported by the National Natural Science Foundation of China (82272145; to H.W.), the Westlake Education Foundation (to H.W.), the Zhejiang Provincial Natural Science Foundation of China under grant number XHD23C1001 (to H.W.), the Harvard/Brigham Nanotechnology Foundation (2022A002721; to W.T.) and the Farokhzad Family Distinguished Chair Foundation (018129; to W.T.). H.W. thanks the Instrumentation and Service Center for Molecular Sciences, Instrumentation and Service Center for Physical Sciences, and Biomedical Research Core Facilities at Westlake University for the assistance with measurements.

Author contributions

H.W. and W.T. conceived the project. Z.Z. performed the in vitro experiments. Z.Z. and D.C. together performed the in vivo experiments and collected the data. Nan Kong, T.X. and J.W. performed some cell experiments. L.Z. and Z.Z. synthesized the compounds. H.Z. conducted the ITC experiments. H.W., Z.Z. and D.C. analysed the data and wrote the paper with input from the other authors. J.O., W.C., Na Kong and W.T. revised and improved the paper. All the authors discussed the results and had agreement on the final version of the paper.

Competing interests

H.W. applied for a patent (CN202411106474) on this platform. W.T. receives consults (or on scientific advisory boards) for, lectured (and received a fee), or conducts sponsored research at Harvard Medical School/Brigham and Women's Hospital for the following entities: Novo Nordisk A/S and Henlius USA Inc. The other authors declare no competing interests.

Additional information

Extended data is available for this paper at https://doi.org/10.1038/s41551-026-01680-0.

Supplementary information The online version contains supplementary material available at https://doi.org/10.1038/s41551-026-01680-0.

Correspondence and requests for materials should be addressed to Wei Tao or Huaimin Wang.

Peer review information *Nature Biomedical Engineering* thanks Octavio Franco, Li-Li Li and the other, anonymous, reviewer(s) for their contribution to the peer review of this work.

https://doi.org/10.1038/s41551-026-01680-0

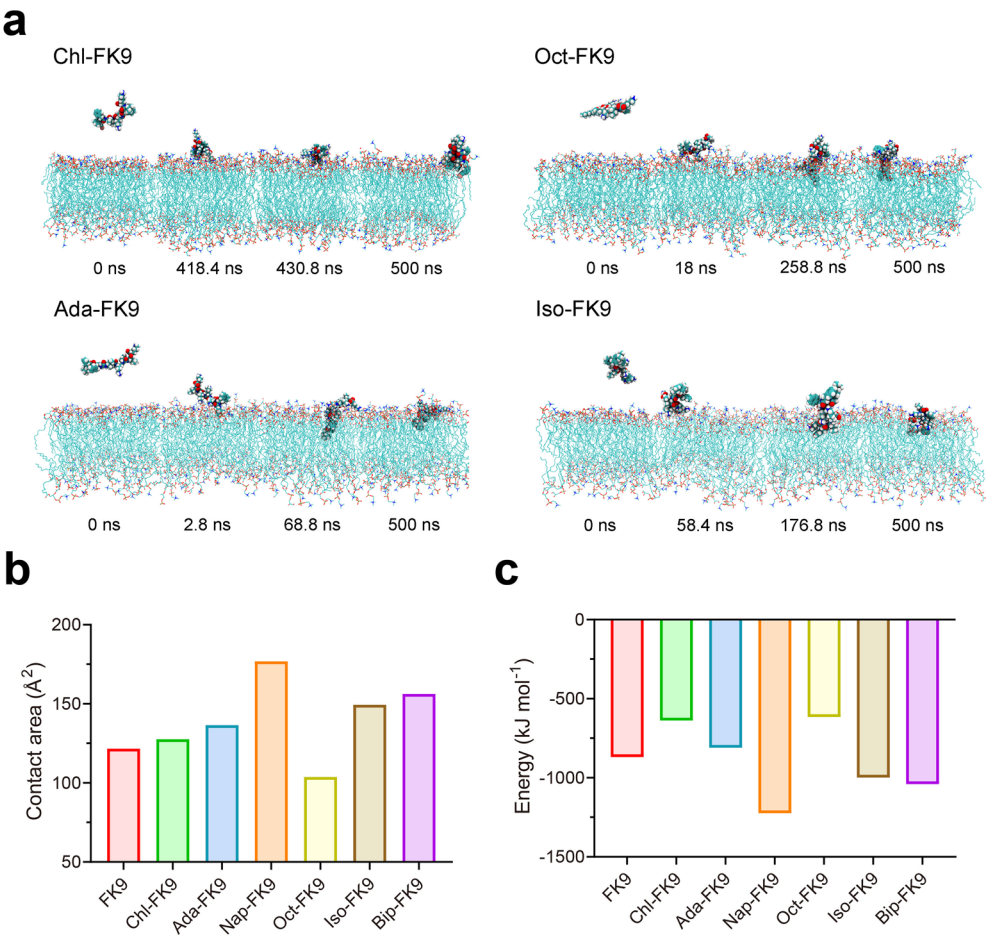

Extended Data Fig. 1 | Molecular dynamics simulation of FK9 modified with these N-terminal groups transmembrane domain. a, Representative configurations of MD simulations of Chl-FK9, Oct-FK9, Ada-FK9, and Iso-FK9 within 500 ns. The beginning state, membrane approach, membrane penetration, and equilibrium stage (500 ns) were shown from left to right. Lipid bilayers composition: PC: PG = 7: 3. **b**, **c**, Contact area (**b**) and energy (**c**) of peptides with phospholipid bilayers at equilibrium time of MD simulations. Chl-FK9 remained outside the bacterial membrane because the charged chlorine atom of Chl-FK9 enhanced the hydrophilicity of the whole system. Only the fat chain in the Oct-FK9 was wholly inserted into the membrane, yielding a low contact area and high energy scope. Because the Nap-FK9 was laid flat on the surface of phospholipid bilayers, the large contact area and low energy scope cannot induce membrane destruction.

https://doi.org/10.1038/s41551-026-01680-0

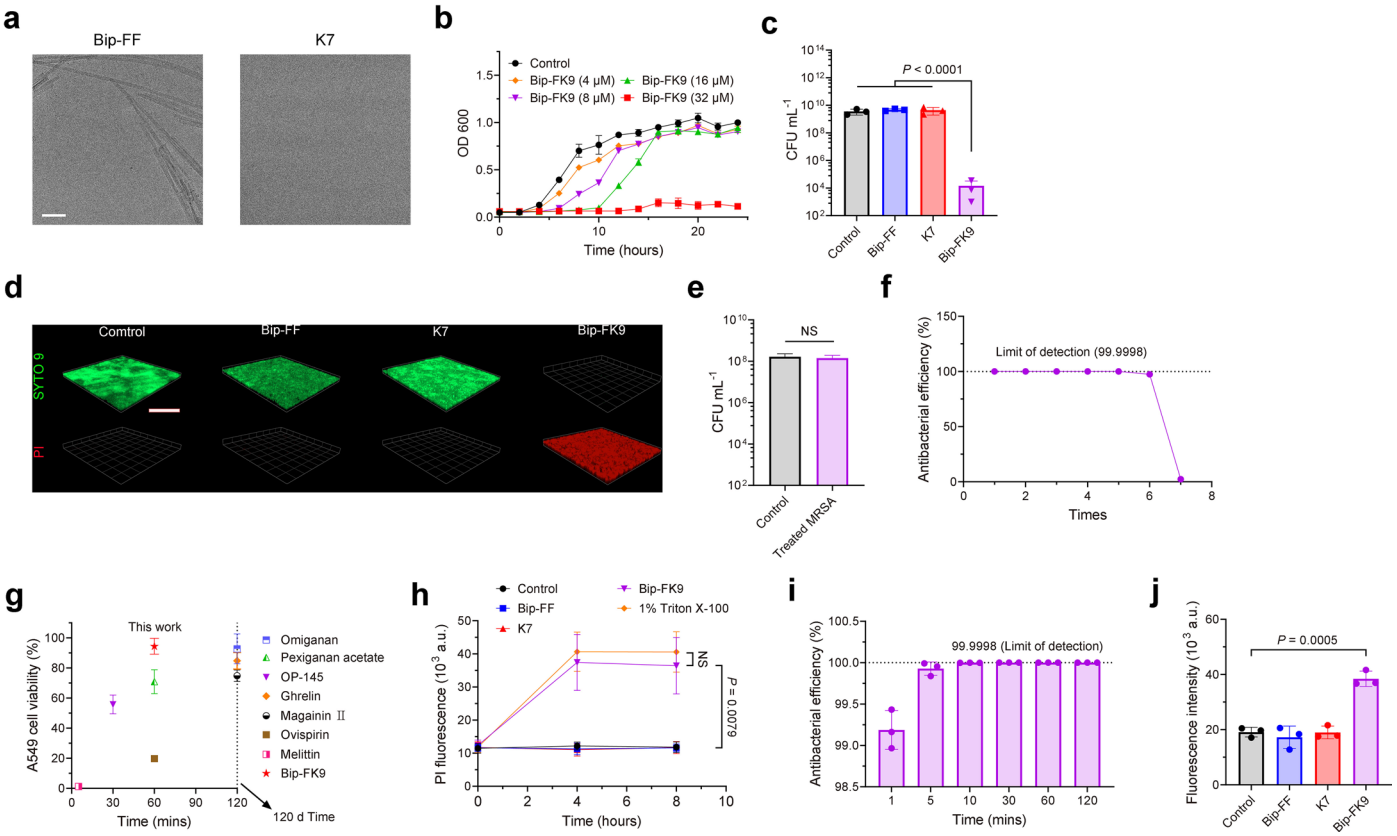

Extended Data Fig. 2 | In vitro antibacterial activity of Bip-FK9. a, The cryo-electron microscope (Cryo-EM) images of Bip-FF and K7 in the PBS buffer. Scale bar, 100 nm. **b**, Growth curves of MRSA under the treatment of Bip-FK9 at different concentrations from 4 to 32 μM. **c**, MRSA viability upon treatment with Bip-FK9 (32 μM) at 8 hours. The minimum detectable concentration of MRSA strains is 1×10^2 CFU mL^{-1}. The data are presented as mean ± s.d. (n = 3). **d**, Fluorescence images of MRSA biofilm treated with Bip-FF, K7, and Bip-FK9. Live bacteria were stained with SYTO9 (green), and dead bacteria were stained with PI (red). Scale bar, 160 μm. **e**, The viability of MRSA under the treatment of the treated MRSA. **f**, The antibacterial efficiency of Bip-FK9 across multiple cycles of use. **g**, The viability of A549 cells was assessed following treatment with Omiganan, Pexiganan acetate, OP-145, Ghrelin, Magainin II, Ovispirin, Melittin, and Bip-FK9 for 24 hours. Additionally, the time required for Bip-FK9 and these classical antimicrobial peptides at a concentration of 128 μM to reduce bacterial counts from 1×10^8 CFU mL^{-1} to the detection limit was evaluated. '120 d time' means greater than or equal to 120 mins. **h**, Dynamic curves of the fluorescence intensity of PI in the treated MRSA solution over time. The 1% Triton X-100 group serves as a positive control. Higher fluorescence signals indicate greater damage to the bacterial membrane. Data are presented as mean ± s.d. (n = 3). **i**, The antibacterial efficiency of Bip-FK9 in the MRSA suspension at different time points. Data are presented as mean ± s.d. (n = 3). **j**, The fluorescence intensity of the ROS probe DCFH-DA in MRSA treated with Bip-FF, K7, and Bip-FK9, respectively. A stronger fluorescence intensity means higher levels of ROS in MRSA. DCFH-DA, 2′,7′-dichlorodihydrofluorescein diacetate. Data are presented as mean ± s.d. (n = 3).

https://doi.org/10.1038/s41551-026-01680-0

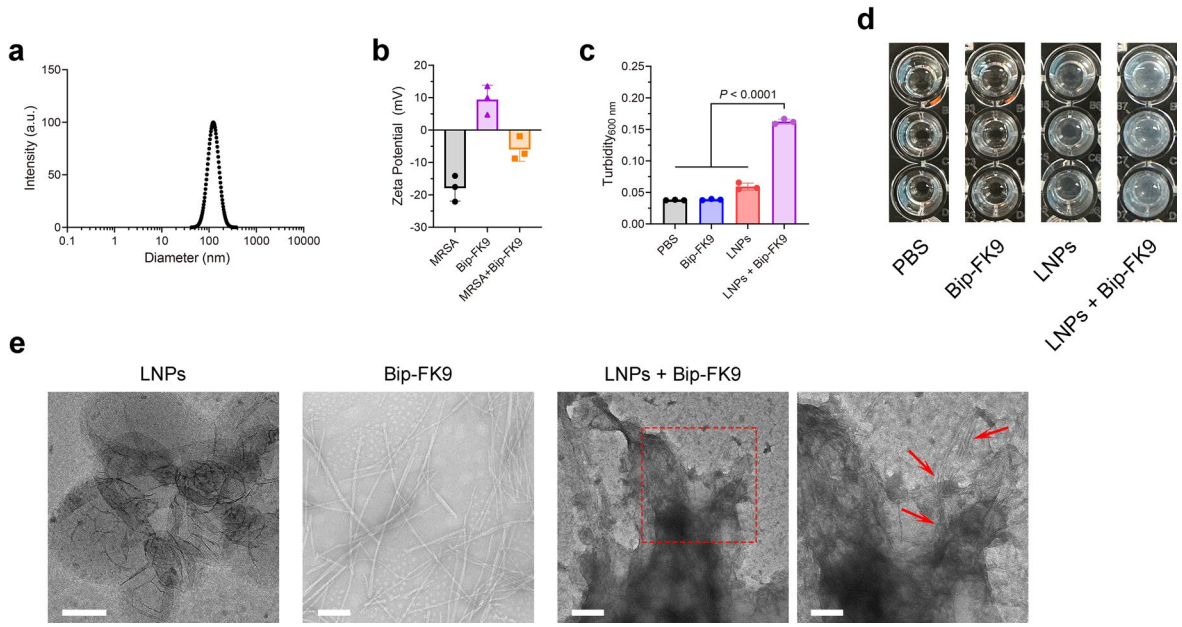

Extended Data Fig. 3 | The interaction between Bip-FK9 and LNPs. a, Size distribution of LNPs measured by a dynamic light scattering (DLS) instrument. **b**, Zeta potential of MRSA, Bip-FK9, and the mixture of Bip-FK9 with MRSA. Individual data are presented as mean ± s.d. (n = 3). **c**, Turbidity measurements at 600 nm for liposome nanoparticle (LNPs) solution with or without the treatment of Bip-FK9. **d**, Optical images of the different groups in **c**. **e**, Transmission electron microscope (TEM) images of LNPs, Bip-FK9, and LNPs mixed with Bip-FK9, respectively. Scale bar in the LNPs image, 100 nm; Scale bar in the Bip-FK9 image, 100 nm; Scale bar in the LNPs + Bip-FK9 image, 200 nm; Scale bar in the enlarged LNPs + Bip-FK9 image, 100 nm. The red arrows indicated Bip-FK9 nanofibers.

https://doi.org/10.1038/s41551-026-01680-0

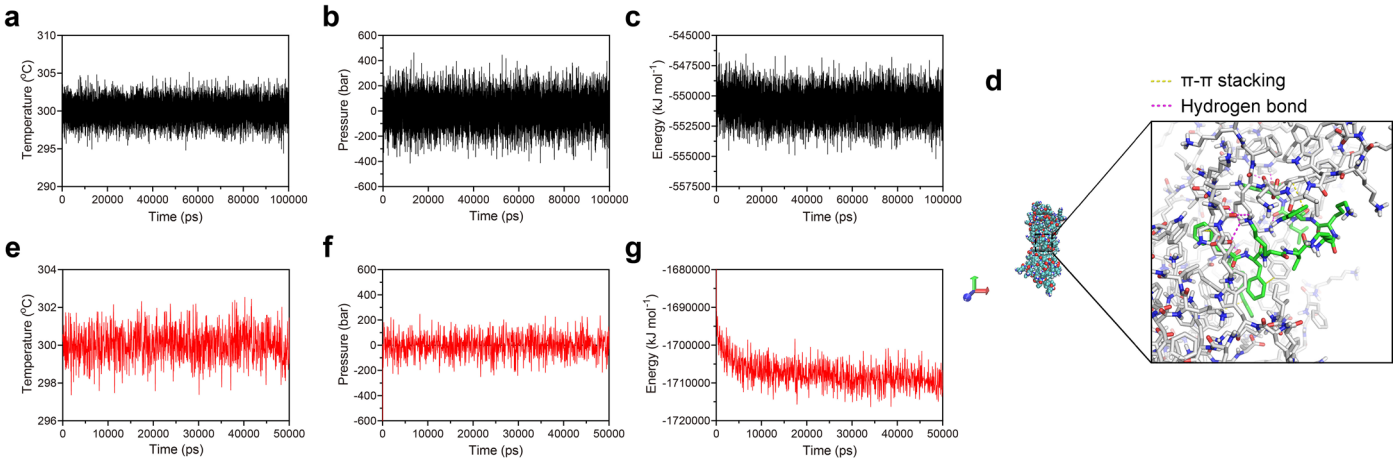

Extended Data Fig. 4 | Molecular dynamics simulation of the Bip-FK9 nanofiber. a-c, Changes in the physical properties of Bip-FK9 assembly over time. (**a**) Temperature, (**b**) pressure, and (**c**) total energy of the system. The representative diagram of Bip-FK9 molecular interaction in the Bip-FK9 nanofiber. **d**, The representative diagram of Bip-FK9 molecular interaction in the Bip-FK9 nanofiber. **e-g**, Changes in the physical properties of the Bip-FK9-BM system over time. (**e**) temperature, (**f**) pressure, and (**g**) total energy of the system.

https://doi.org/10.1038/s41551-026-01680-0

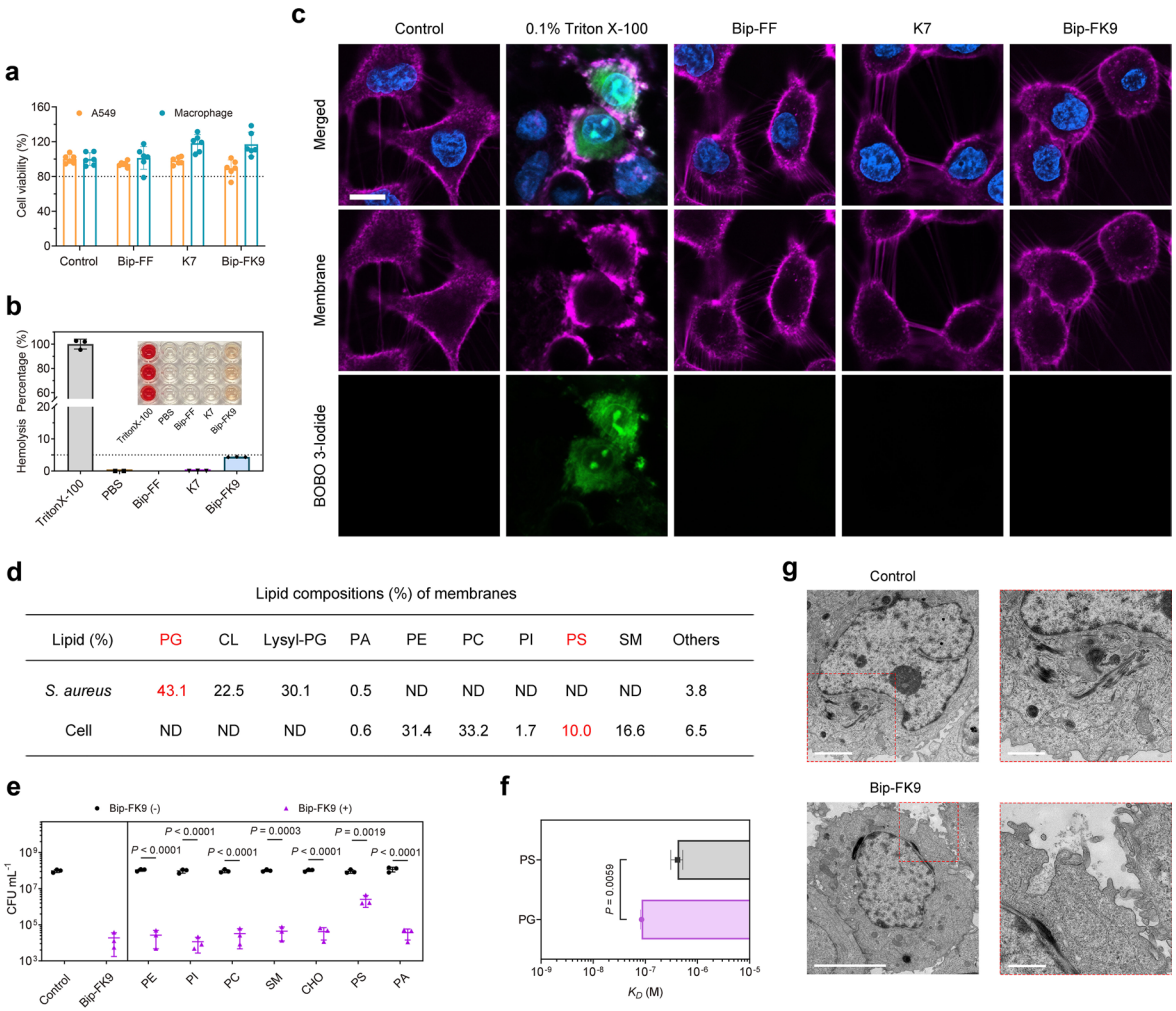

Extended Data Fig. 5 | The cytotoxicity of Bip-FK9 and the mechanism of action of Bip-FK9 on mammalian cell membranes. a, Cell viability of two cell lines (A549 and RAW 264.7) in the presence of Bip-FK9, Bip-FF, and K7, respectively. Data are presented as mean ± s.d. (n = 6). **b**, Haemolytic activity of Bip-FK9 (320 μM), Bip-FF (320 μM), and K7 (320 μM), respectively. Data are presented as mean ± s.d. (n = 3). **c**, The CLSM images of A549 cells treated with 0.1% Triton X-100 (the positive control), Bip-FF, K7, and Bip-FK9, respectively. Scale bar, 10 μm. Blue represents the nucleus and purple is cell membrane, respectively. BOBO 3-Iodide (green), a fluorescent dye, cannot penetrate intact cell membranes but can enter cells when membranes are damaged, allowing it to stain nucleic acids. **d**, A representative diagram illustrating lipid compositions of *S. aureus* membrane and mammalian plasma membrane (% of total phospholipids). ND, not determined. **e**, Changes in bacterial concentrations after the treatment of Bip-FK9 in the presence of mammalian plasma membrane components. Data are presented as mean ± s.d. (n = 3). **f**, The statistical analysis of the dissociation constants K_D between Bip-FK9 and lipids (PG and PS). **g**, The TEM images of A549 cells without or with the treatment of Bip-FK9. Scale bar in the image of the Control group, 2 μm; Scale bar in the enlarged image of the Control group, 1 μm. Scale bar in the image of the Bip-FK9 group, 5 μm; Scale bar in the enlarged image of the Bip-FK9 group, 1 μm. Statistical analysis in e and f was performed using an unpaired, two-tailed Student's t-test.

https://doi.org/10.1038/s41551-026-01680-0

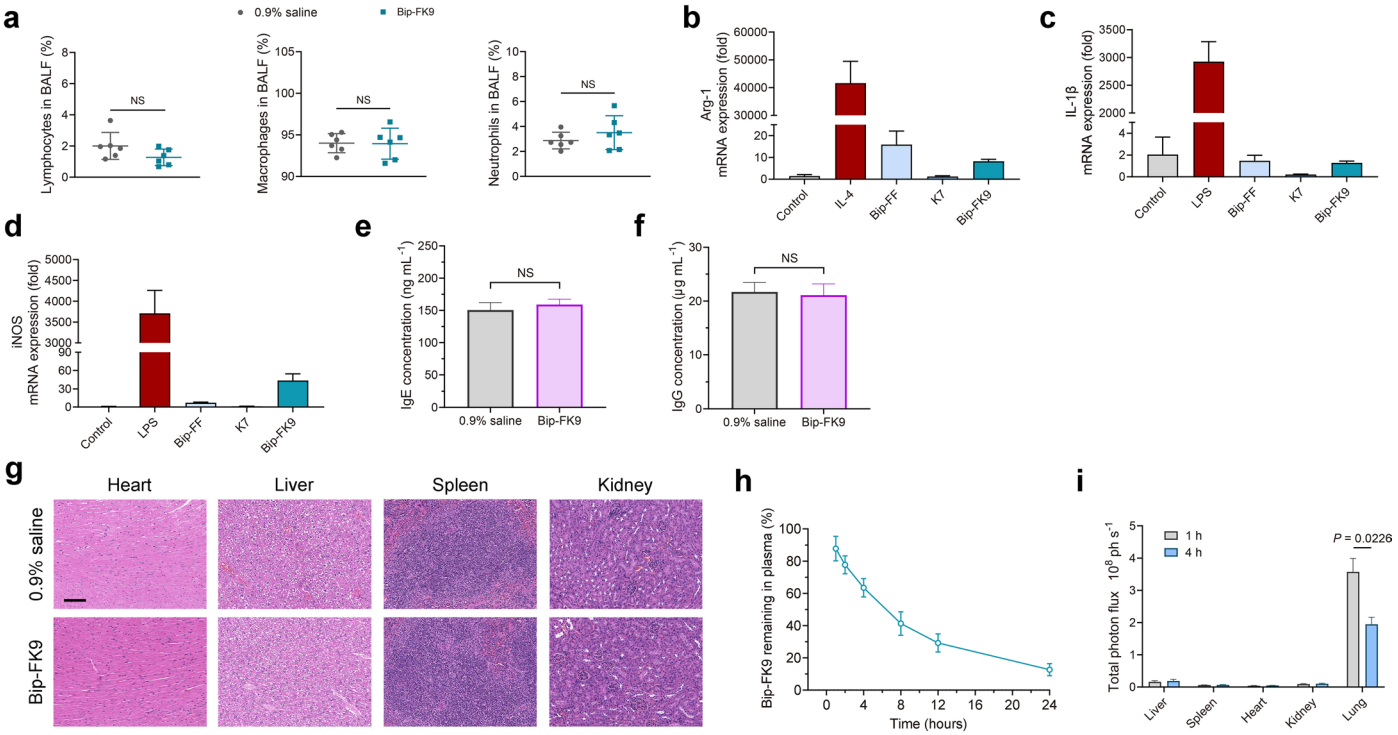

Extended Data Fig. 6 | In vivo biosafety of Bip-FK9. a, Quantification of cellularity in the BALF from the mice treated with 0.9% saline or Bip-FK9. The percentage of lymphocytes (left), macrophages (middle), and neutrophils (right) were quantified through Giemsa staining. Individual data are presented as mean ± s.d. (n = 6). **b-d**, qPCR quantification of mRNA level of proteins related to Macrophage M1/M2 polarization. RAW264.7 cells were co-incubated with LPS (positive control) or IL-4 (positive control) peptides for 24 hours. Untreated cells were set as a negative control. Then, cells were collected for RNA extraction, cDNA synthesis, and quantification of the mRNA expression level of Arg-1 (**b**), IL-1β (**c**), and iNOS (**d**). Individual data are presented as mean ± s.d. (n = 3). **e**, **f**, The concentration of IgE (**e**), and IgG (**f**) in the serum from mice that received consecutive 7 days of Bip-FK9 nebulization. Data are presented as mean ± s.d. (n = 6). **g**, Representative histological images of major organs. Scale bar, 100 μm. **h**, The stability of Bip-FK9 in mouse plasma. Individual data are presented as mean ± s.d. (n = 3). **i**, Quantification of the total flux of each organ in the mice was administered with Bip-FK9-Cy5.5 via nebulization to the lungs. The Cy5.5 fluorescence was measured in total photon flux (ph s^{-1}). Individual data are presented as mean ± s.d. (n = 4). Statistical analysis of data in **a**, **e**, **f**, and **i** was performed using a two-tailed Student's t-test.

https://doi.org/10.1038/s41551-026-01680-0

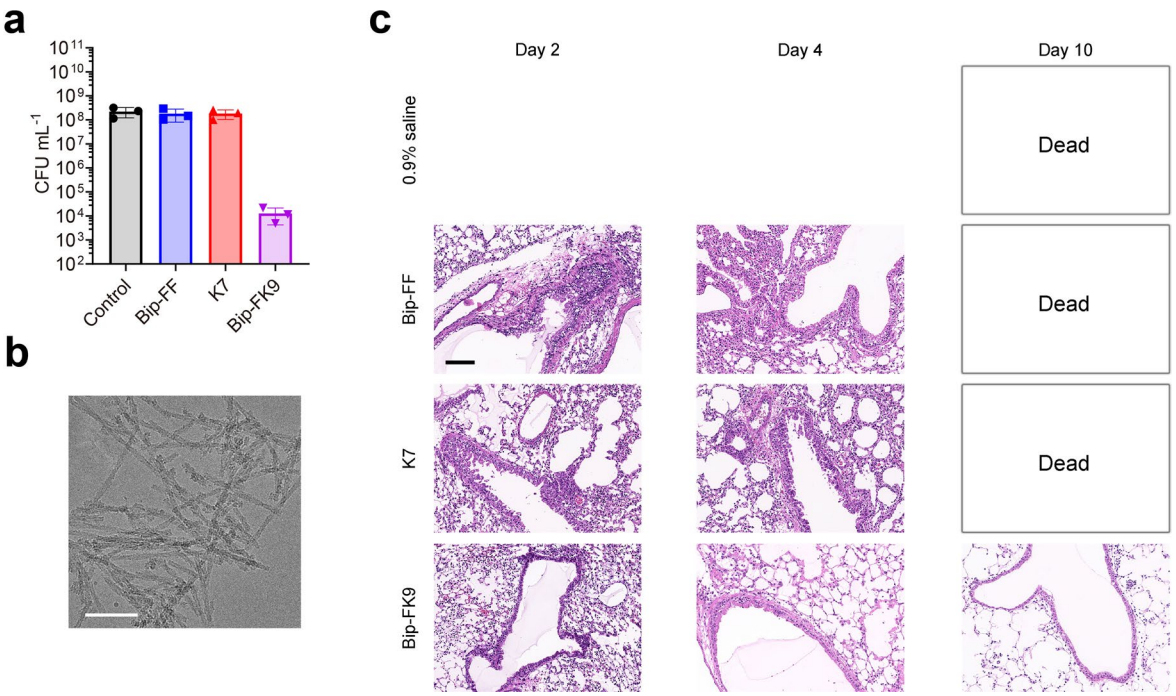

Extended Data Fig. 7 | Evaluation of the in vivo anti-infective activity of Bip-FK9. a, Colony forming unit (CFU) concentration of MRSA under the treatment of Bip-FF (128 μM), K7 (128 μM), and Bip-FK9 (128 μM) in artificial mucus in vitro. Individual data are presented as mean ± s.d. (n = 3). **b**, The Cryo-EM image of Bip-FK9 solution obtained from a mouse nebulizer. Scale bar, 100 nm. **c**, Representative histological images (H&E staining) of lung sections. Lung tissues were harvested from mice treated with the peptide groups and the 0.9% saline group on days 2, 4, and 10. Untreated mice (healthy) were set as a negative control. Scale bar, 100 μm.

nature portfolio

Corresponding author(s): Wei Tao, Huaimin Wang

Last updated by author(s): Jan 29, 2026

Reporting Summary

Nature Portfolio wishes to improve the reproducibility of the work that we publish. This form provides structure for consistency and transparency in reporting. For further information on Nature Portfolio policies, see our Editorial Policies and the Editorial Policy Checklist.

Statistics

For all statistical analyses, confirm that the following items are present in the figure legend, table legend, main text, or Methods section.

n/a	Confirmed	
☐	☒	The exact sample size (*n*) for each experimental group/condition, given as a discrete number and unit of measurement
☐	☒	A statement on whether measurements were taken from distinct samples or whether the same sample was measured repeatedly
☐	☒	The statistical test(s) used AND whether they are one- or two-sided *Only common tests should be described solely by name; describe more complex techniques in the Methods section.*
☒	☐	A description of all covariates tested
☒	☐	A description of any assumptions or corrections, such as tests of normality and adjustment for multiple comparisons
☐	☒	A full description of the statistical parameters including central tendency (e.g. means) or other basic estimates (e.g. regression coefficient) AND variation (e.g. standard deviation) or associated estimates of uncertainty (e.g. confidence intervals)
☐	☒	For null hypothesis testing, the test statistic (e.g. *F*, *t*, *r*) with confidence intervals, effect sizes, degrees of freedom and *P* value noted *Give P values as exact values whenever suitable.*
☒	☐	For Bayesian analysis, information on the choice of priors and Markov chain Monte Carlo settings
☒	☐	For hierarchical and complex designs, identification of the appropriate level for tests and full reporting of outcomes
☒	☐	Estimates of effect sizes (e.g. Cohen's *d*, Pearson's *r*), indicating how they were calculated

Our web collection on statistics for biologists contains articles on many of the points above.

Software and code

Policy information about availability of computer code

Data collection	The fluorescent intensity of NPN (λex = 350 nm, λem = 420 nm) and the membrane-potential-sensitive dye DiSC3(5) was monitored by Spectrofluorometer (Edinburgh, F55). Molecular dynamic simulations were performed in Gromacs 2018.3. The maximum absorption wavelength (λmax) of Rhodamine 6G was measured by Microplate Reader (Varioskan Lux, ThermoFisher, USA). The morphology of the peptides and bacteria was observed by cryo-electron microscopy (Cyro-EM, CRYO-EM001, Thermo Fisher). Zeta potential was measured by a Zeta Nanosizer (LHA19110041, Brookhaven). The CD data was collected using spectrometer V100 (Rudolph Autopol IV-T). ITC (MicroCal PEAQ-ITC, Malvern Panalytical Limited) was used to evaluate the binding affinity between DOPG and Bip-FK9. All spectra of the BipF-FK9 blended with DOPG were measured using 600 MHz solution NMR spectrometer with cryo-probe (AVANCE NEO, Bruker BioSpin). The morphology of cells was visualized by fluorescence microscopy (Evos FL Auto 2, Invitrogen by Thermo Fisher Scientific). qPCR was performed subsequently on a Step One Plue Real-Time PCR system (Applied Biosystems) using SYBR Premix Ex Taq™ (TAKARA). The confocal images were collected using confocal laser scanning microscopy (CLSM 800, Zeiss, Germany).
Data analysis	Graphpad Prism 9 was used for statistical analysis. Phospholipid bilayer model was constructed using CHARMM-GUI. The ITC data was analysed by MicroCal PEAQ-ITC, Malvern Panalytical Limited. NMR data was analysized by the MestReNova 14.2 sofeware.

For manuscripts utilizing custom algorithms or software that are central to the research but not yet described in published literature, software must be made available to editors and reviewers. We strongly encourage code deposition in a community repository (e.g. GitHub). See the Nature Portfolio guidelines for submitting code & software for further information.

Data

Policy information about availability of data

All manuscripts must include a data availability statement. This statement should provide the following information, where applicable:

- Accession codes, unique identifiers, or web links for publicly available datasets
- A description of any restrictions on data availability
- For clinical datasets or third party data, please ensure that the statement adheres to our policy

The main data supporting the results in this study are available within the paper and its Supplementary Information flies.

Research involving human participants, their data, or biological material

Policy information about studies with human participants or human data. See also policy information about sex, gender (identity/presentation), and sexual orientation and race, ethnicity and racism.

Reporting on sex and gender	*Use the terms sex (biological attribute) and gender (shaped by social and cultural circumstances) carefully in order to avoid confusing both terms. Indicate if findings apply to only one sex or gender; describe whether sex and gender were considered in study design; whether sex and/or gender was determined based on self-reporting or assigned and methods used.* *Provide in the source data disaggregated sex and gender data, where this information has been collected, and if consent has been obtained for sharing of individual-level data; provide overall numbers in this Reporting Summary. Please state if this information has not been collected.* *Report sex- and gender-based analyses where performed, justify reasons for lack of sex- and gender-based analysis.*
Reporting on race, ethnicity, or other socially relevant groupings	*Please specify the socially constructed or socially relevant categorization variable(s) used in your manuscript and explain why they were used. Please note that such variables should not be used as proxies for other socially constructed/relevant variables (for example, race or ethnicity should not be used as a proxy for socioeconomic status).* *Provide clear definitions of the relevant terms used, how they were provided (by the participants/respondents, the researchers, or third parties), and the method(s) used to classify people into the different categories (e.g. self-report, census or administrative data, social media data, etc.)* *Please provide details about how you controlled for confounding variables in your analyses.*
Population characteristics	*Describe the covariate-relevant population characteristics of the human research participants (e.g. age, genotypic information, past and current diagnosis and treatment categories). If you filled out the behavioural & social sciences study design questions and have nothing to add here, write "See above."*
Recruitment	*Describe how participants were recruited. Outline any potential self-selection bias or other biases that may be present and how these are likely to impact results.*
Ethics oversight	*Identify the organization(s) that approved the study protocol.*

Note that full information on the approval of the study protocol must also be provided in the manuscript.

Field-specific reporting

Please select the one below that is the best fit for your research. If you are not sure, read the appropriate sections before making your selection.

☒ Life sciences ☐ Behavioural & social sciences ☐ Ecological, evolutionary & environmental sciences

For a reference copy of the document with all sections, see nature.com/documents/nr-reporting-summary-flat.pdf

Life sciences study design

All studies must disclose on these points even when the disclosure is negative.

Sample size	Sample sizes for the animal studies were based on prior work, without using additional statistical estimations.
Data exclusions	No data were excluded.
Replication	All experiments were independently repeated at least three times with similar results. The number of repetitions for each experiment is shown in its own legend.
Randomization	The animals were randomly allocated to different experimental groups.
Blinding	No blinding measures were performed, and all data were processed by authors.

Reporting for specific materials, systems and methods

We require information from authors about some types of materials, experimental systems and methods used in many studies. Here, indicate whether each material, system or method listed is relevant to your study. If you are not sure if a list item applies to your research, read the appropriate section before selecting a response.

Materials & experimental systems

n/a	Involved in the study
☒	☐ Antibodies
☐	☒ Eukaryotic cell lines
☒	☐ Palaeontology and archaeology
☐	☒ Animals and other organisms
☒	☐ Clinical data
☒	☐ Dual use research of concern
☒	☐ Plants

Methods

n/a	Involved in the study
☒	☐ ChIP-seq
☒	☐ Flow cytometry
☒	☐ MRI-based neuroimaging

Eukaryotic cell lines

Policy information about cell lines and Sex and Gender in Research

Cell line source(s)	A549 and RAW 264.7 cells were purchased from the American Type Culture collection (ATCC).
Authentication	None of the cell lines were authenticated.
Mycoplasma contamination	All cell lines tested negative for mycoplasma contamination.
Commonly misidentified lines (See ICLAC register)	No commonly misidentified lines were used in this study.

Animals and other research organisms

Policy information about studies involving animals; ARRIVE guidelines recommended for reporting animal research, and Sex and Gender in Research

Laboratory animals	BALB/C were male and 8 weeks old.
Wild animals	The study did not involve wild animals.
Reporting on sex	All animals were male.
Field-collected samples	The study did not involve samples collected from the field.
Ethics oversight	The Institutional Animal Care and Use Committee (IACUC) and the Westlake University Animal Care, Westlake University.

Note that full information on the approval of the study protocol must also be provided in the manuscript.

Plants

Seed stocks	*Report on the source of all seed stocks or other plant material used. If applicable, state the seed stock centre and catalogue number. If plant specimens were collected from the field, describe the collection location, date and sampling procedures.*
Novel plant genotypes	*Describe the methods by which all novel plant genotypes were produced. This includes those generated by transgenic approaches, gene editing, chemical/radiation-based mutagenesis and hybridization. For transgenic lines, describe the transformation method, the number of independent lines analyzed and the generation upon which experiments were performed. For gene-edited lines, describe the editor used, the endogenous sequence targeted for editing, the targeting guide RNA sequence (if applicable) and how the editor was applied.*
Authentication	*Describe any authentication procedures for each seed stock used or novel genotype generated. Describe any experiments used to assess the effect of a mutation and, where applicable, how potential secondary effects (e.g. second site T-DNA insertions, mosiacism, off-target gene editing) were examined.*